

Review

In Situ Characterization Techniques Based on Synchrotron Radiation and Neutrons Applied for the Development of an Engineering Intermetallic Titanium Aluminide Alloy

Petra Erdely ^{1,*}, Thomas Schmoelzer ^{2,†}, Emanuel Schwaighofer ^{2,‡}, Helmut Clemens ², Peter Staron ³, Andreas Stark ³, Klaus-Dieter Liss ⁴ and Svea Mayer ²

Received: 30 November 2015; Accepted: 23 December 2015; Published: 4 January 2016

Academic Editor: Hugo F. Lopez

- ¹ Recipient of a DOC Fellowship of the Austrian Academy of Sciences at the Department of Physical Metallurgy and Materials Testing, Montanuniversität Leoben, Roseggerstraße 12, 8700 Leoben, Austria
- ² Department of Physical Metallurgy and Materials Testing, Montanuniversität Leoben, Roseggerstraße 12, 8700 Leoben, Austria; thomas.schmoelzer@ch.abb.com (T.S.); emanuel.schwaighofer@alumni.unileoben.ac.at (E.S.); helmut.clemens@unileoben.ac.at (H.C.); svea.mayer@unileoben.ac.at (S.M.)
- ³ Institute of Materials Research, Helmholtz-Zentrum Geesthacht, Max Planck-Straße 1, 21502 Geesthacht, Germany; peter.staron@hzg.de (P.S.); andreas.stark@hzg.de (A.S.)
- ⁴ The Bragg Institute, Australian Nuclear Science and Technology Organisation, New Illawarra Road, Lucas Heights, NSW 2234, Australia; kdl@ansto.gov.au
- * Correspondence: petra.erdely@unileoben.ac.at; Tel.: +43-3842-402-4213; Fax: +43-3842-402-4202
- † Current address: ABB Corporate Research Center, Segelhofstrasse 1K, 5405 Baden-Dättwil, Switzerland.
- ‡ Current address: Böhler Edelstahl GmbH & Co KG, Mariazellerstraße 25, 8605 Kapfenberg, Austria.

Abstract: Challenging issues concerning energy efficiency and environmental politics require novel approaches to materials design. A recent example with regard to structural materials is the emergence of lightweight intermetallic TiAl alloys. Their excellent high-temperature mechanical properties, low density and high stiffness constitute a profile perfectly suitable for their application as advanced aero-engine turbine blades or as turbocharger turbine wheels in next-generation automotive engines. As the properties of TiAl alloys during processing as well as during service are dependent on the phases occurring, detailed knowledge of their volume fractions and distribution within the microstructure is of paramount importance. Furthermore, the behavior of the individual phases during hot deformation and subsequent heat treatments is of interest to define reliable and cost-effective industrial production processes. *In situ* high-energy X-ray diffraction methods allow tracing the evolution of phase fractions over a large temperature range. Neutron diffraction unveils information on order-disorder transformations in TiAl alloys. Small-angle scattering experiments offer insights into the materials' precipitation behavior. This review attempts to shine a light on selected *in situ* diffraction and scattering techniques and the ways in which they promoted the development of an advanced engineering TiAl alloy.

Keywords: titanium aluminides based on γ -TiAl; high-energy X-ray diffraction; phase transformations; neutron diffraction; order/disorder transformations; small-angle scattering; thermo-mechanical processing; heat treatments; microstructure evolution

1. Introduction

Presently, jet engines are the prevalent form of propulsion systems in commercial airplanes. Increasing economic and environmental pressure, however, has triggered an ever-rising awareness

of the issues associated with the consumption of fossil fuels. As a result, a growing demand for environmentally-friendly engine options has emerged. Substantial improvements in fuel efficiency, noise and greenhouse gas emissions can be effected by reducing the weight of selected components. This end can be achieved either by adapting the overall design or by implementing advanced structural materials that exhibit mechanical properties equal to conventional materials while having lower densities. The latter approach has been realized successfully, for instance, by installing intermetallic titanium aluminide turbine blades in the last stages of the low-pressure turbine of the GENx™ engine by General Electrics [1]. In this way, the twice as heavy nickel-base superalloy blades could be replaced. Pratt & Whitney recently introduced TiAl turbine blades in their so-called Geared Turbofan™ engine, which will be used to power the Airbus A320neo family besides other aircrafts [2,3].

Intermetallic titanium aluminides based on the ordered γ -TiAl phase provide a set of properties well suited for structural high-temperature applications. At a density of about $4 \text{ g} \cdot \text{cm}^{-3}$, they combine a high melting point with a high elastic modulus. Strength and creep properties, as well as oxidation and burn resistance are good, even at high temperatures [4–9]. Capable of withstanding extreme conditions, titanium aluminides have found applications in the automotive and aircraft engine industry, as reported in [10,11]. As engine valves in sports and racing cars, as turbocharger turbine wheels and as low-pressure turbine blades in jet engines, they are expected to replace conventional high-temperature materials of high density in a temperature range up to $750 \text{ }^\circ\text{C}$ [4,6–8,10–19]. During the last few decades, considerable efforts have been made to develop γ -TiAl-based alloys suitable for service in these demanding areas, while being economically competitive at the same time. Various processing routes and alloy compositions have been studied intensively [9,12,20,21].

Among the recently-developed third-generation titanium aluminide alloys, the β -solidifying TNM alloys in particular strive to overcome processing-related difficulties inherent to brittle intermetallic materials [11,20]. With a nominal composition of Ti–43.5Al–4Nb–1Mo–0.1B (at. %), their distinct characteristic is an adjustable β/β_0 phase fraction, which is stabilized by the alloying elements Nb and Mo (hence the name TNM) [20,22]. At elevated temperatures, a substantial volume fraction of the disordered β -Ti(Al) phase (A2 structure) is obtained [23]. The presence of this phase improves the material's hot workability by providing a sufficient number of independent slip systems [7,24–27]. Furthermore, it allows near-conventional hot-die forging due to an enlarged processing window [28,29]. At service temperatures, however, the ordered β_0 -TiAl phase (B2 structure) reduces the material's creep strength significantly [11,25]. Heat treatments must be applied after forging to reduce the β_0 phase fraction to a minimum. By simultaneously adjusting the material's microstructure, attractive mechanical properties can be tailored.

Depending on the temperature profile of the heat treatment applied, as well as on the material's chemical composition, different microstructural features can be adjusted in TiAl alloys, ranging from near gamma (NG) and duplex (D) microstructures over nearly-lamellar (NL) to fully-lamellar (FL) microstructures [6,7,10,30]. FL microstructures exhibit the best creep properties at the expense of a diminished room-temperature ductility [31,32]. NL microstructures offer the most balanced properties, providing strong creep resistance and moderate ductility at ambient temperature [33]. In Figure 1a, the NL microstructure of a heat-treated TNM alloy is shown. The image was obtained by means of scanning electron microscopy (SEM). In the back-scatter electron (BSE) mode, the three main phases α_2 , β_0 and γ can be distinguished by their differing contrast: β_0 appears brightest, γ darkest and α_2 in an intermediate contrast. The insert in the right upper corner represents a high-resolution transmission electron microscopy (HRTEM) image of the lamellae within an α_2/γ colony.

A further outstanding characteristic of TNM alloys is their solidification pathway via the β phase [28]. Due to an intrinsic grain refinement, the solidified microstructure appears equiaxed and free from a significant casting texture [34]. Additionally, as opposed to the microstructure after peritectic solidification, the material is nearly segregation-free. In spite of the given advantages, cast microstructures are frequently rather coarse. Optimized heat treatments are necessary to adjust the material's microstructure [21,35,36] and properties [37].

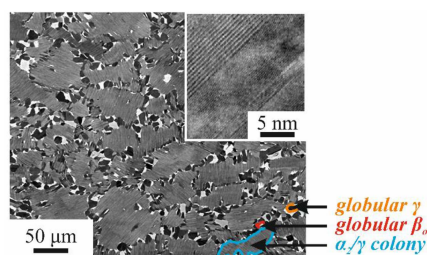


Figure 1. Nearly lamellar microstructure of a nominal TNM alloy (SEM-back-scatter electron (BSE) image) The microstructure, which was arranged during a two-step heat treatment, consists of lamellar α_2/γ colonies surrounded by globular γ and β_0 grains (dark and bright contrast, respectively). The insert (HRTEM image) features a lamellar colony. (Reproduced with permissions from Reference [11]. Copyright © Wiley-VCH Verlag GmbH & Co. KGaA, Weinheim, Germany, 2013).

Currently, so-called TNM⁺ alloys are attracting notice, as the creep properties, as well as the microstructural stability can be increased as compared to regular TNM alloys. To this end, harmonized additions of C and Si are accommodated in the alloy composition [38,39]. Carbon and Si are known to act as solid solution strengtheners [40,41]. In addition to this, precipitates (cubic Ti₃AlC, hexagonal Ti₂AlC or Ti₅Si₃) tend to form during high-temperature creep experiments [42–44]. Detailed knowledge of the associated precipitation processes, however, is still needed for their deliberate application to improve a material's high-temperature properties.

The basis for addressing such research questions is provided by a profound understanding of the thermodynamics and kinetics of the phase transformations occurring. The resultant control over the composition and arrangement of the phases prevalent in a material allows the targeted adjustment of its properties. In the case of TiAl alloys, conventional *ex situ* characterization methods, although generally available and rather cost effective, encounter certain difficulties. First, the alloy system itself is rendered complex by a multitude of phases and phase transformations, whose occurrence and exact transformation temperatures are strongly dependent on the material's chemical composition [28]. Thermodynamic calculations cannot, at present, be consulted, except for trends, since commercially-available Ti–Al databases have been found to be unreliable in describing phase diagrams containing high amounts of β/β_0 -stabilizing elements [11]. Secondly, ordering reactions exhibit extremely fast kinetics [45]. Thus, the disordered high-temperature state cannot be preserved for study at room temperature even by rapid quenching. Phase fractions might change as well, introducing errors in the attempted investigation of high-temperature states in heat-treated and water-quenched specimens [46]. For detailed information on the advantages and limitations of the method of quantitative phase evaluation through microscopic images, the reader is referred to [47]. Thirdly, SEM and X-ray diffraction using laboratory X-ray sources usually suffer from the restriction to the surface or to near-surface areas of the specimens. These areas might in some cases not yield sufficient grain statistics or, following extended heat treatments, be affected by the formation of an α case, an Al-depleted near-surface region of several μm in thickness [48–50]. Transmission electron microscopy (TEM) is also restricted to small sample volumes.

Diffraction and scattering techniques using high-energy X-rays and neutrons have been shown to overcome most of the problems mentioned above [48,49,51,52]. Having been used as a tool for material characterization since the early beginnings of research activities on TiAl alloys [46,53–59], they have successfully promoted the development of the alloy in various aspects (Figure 2). In this review, selected *in situ* characterization techniques shall be presented through a set of recent examples, highlighting the ways in which they contributed to the development of TNM alloys. The topics addressed range from fundamental research questions, such as the establishment of phase diagrams or the investigation of transformation and precipitation kinetics, to processing- or application-related

problems, such as the hot deformation behavior of TNM alloys or the adjustment of optimized microstructures during heat treatments (Figure 2).

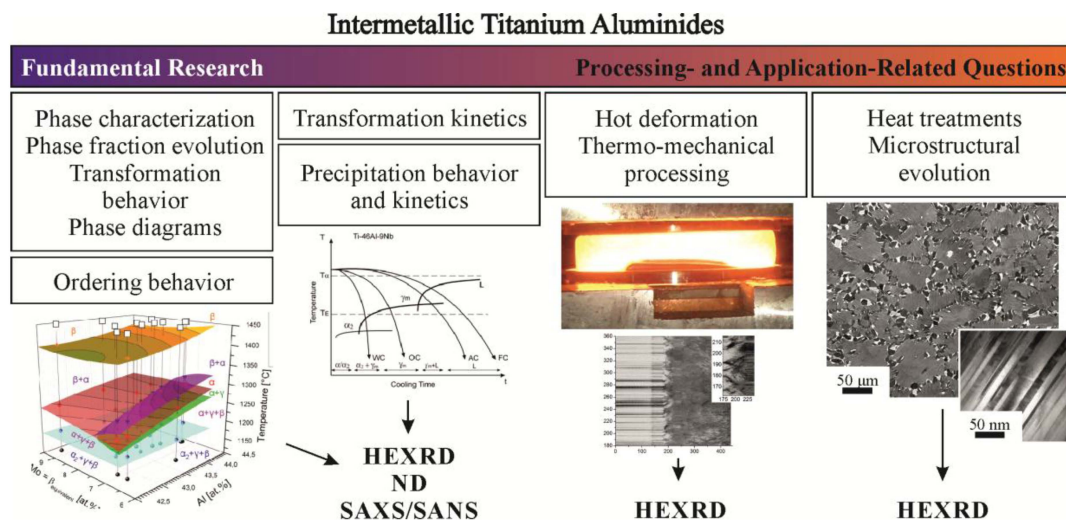


Figure 2. Scheme of the application range of *in situ* characterization techniques based on synchrotron radiation and neutrons in the development of intermetallic titanium aluminides. Neutron diffraction (ND), high-energy X-ray diffraction (HEXRD), and small-angle scattering methods (small-angle X-ray scattering (SAXS)/small-angle neutron scattering (SANS)) address a wide variety of aspects, which cover fundamental research questions, as well as processing- or application-related problems. All aspects, which are illustrated by representative images, are discussed in the present review with a focus on β -solidifying TNM alloys.

2. Peculiarities in the Investigation of Titanium Aluminide Alloys Using X-rays and Neutrons

Their different nature notwithstanding, X-rays and neutrons are both suited for diffraction and scattering experiments in materials science [60]. While neutrons, which possess a mass, are described as particle waves, massless X-rays (photons) represent electromagnetic radiation. Consequently, their modes of interaction with the material under investigation differ. Neutrons interact predominantly with the nuclei of the atoms. X-rays, on the other hand, are scattered by their electrons. This leads to different cross-sections and atomic form factors, while the mathematics derived to describe the scattering of X-rays and neutrons from matter are basically the same.

The description of the scattering of X-rays and neutrons from condensed matter includes the contributions of all atoms in the form of a discrete sum. Thereby, the phase difference due to different positions of the atoms within the ensemble is embraced. If several elements are distributed randomly on a crystal lattice, a virtual atom with a mean scattering length is conceived for the calculation of the structure factor $F_{hkl}(\mathbf{G})$. \mathbf{G} is the scattering vector with Miller indices hkl . Superstructure reflections forbidden by the structure factor do not appear in disordered crystals. The disordered state results in phase factors of equal magnitude, but of opposite sign, causing the corresponding reflections to vanish. For ordered structures, each atom is included in the calculation of $F_{hkl}(\mathbf{G})$ regarding its specific position in the crystal. If different elements possess different scattering lengths, the structure factor for the formerly forbidden reflections hence attains a finite value. This case defines so-called superstructure reflections, which can be observed in the diffraction pattern.

In this regard, TiAl alloys feature an additional, yet useful peculiarity. Since the neutron scattering lengths of Ti (-3.438 fm) and Al (3.449 fm) [61] happen to be almost equal in magnitude but of opposite sign, disordered phases, in which the ratio Ti:Al is close to one, yield only very weak diffraction peaks, because the average scattering length approaches zero. In ordered Ti–Al crystals, the calculated $F_{hkl}(\mathbf{G})$ are close to zero if scattering lengths add up, *i.e.*, for fundamental reflections. The calculation of $F_{hkl}(\mathbf{G})$

for superstructure reflections, however, results in large structure factors, because they contain the difference of scattering lengths of each site. High intensities are obtained, emphasizing the presence of ordered structures (Figure 3a). When X-rays are used to probe the material (Figure 3b), an inverse situation emerges, as the X-ray scattering lengths of Ti and Al are of equal sign, but, due to their different atomic numbers ($Z_{\text{Ti}} = 22$, $Z_{\text{Al}} = 13$), of different magnitude. Superstructure reflections exhibit low intensities, whereas fundamental reflections appear strong. Since these statements are valid for all prevalent phases, neutron and X-ray diffraction are in fact most complementary techniques if applied to intermetallic TiAl alloys. While neutron diffraction offers distinct advantages for the investigation of order/disorder transitions, X-ray diffraction can be employed to study phase transformations and phase fraction evolutions, in which the fundamental reflections play a major role.

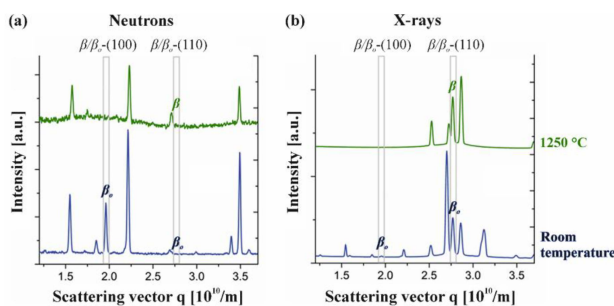


Figure 3. Diffraction patterns of a TNM alloy obtained by (a) neutron and (b) X-ray diffraction at elevated temperatures (top), as well as at room temperature (bottom) [62]. Differences between the patterns of the ordered β_0 phase at room temperature and of its disordered form β at 1250 °C are exemplarily accentuated. In the case of neutron scattering, the β -(100) superstructure peak appears strong, whereas the fundamental β -(110) peak is hardly discernible from the background. In the case of X-rays, the fundamental peak exhibits a high intensity, while the superstructure peak at room temperature shows only a small intensity.

3. *In Situ* Studies of Phase Evolutions

3.1. HEXRD: State-of-the-Art Instrumental Setup

For *in situ* investigations of the phase transformation behavior of titanium aluminides, high-energy X-ray diffraction (HEXRD) has evolved into a powerful and versatile tool [48,50,51,63–66]. At synchrotron radiation sources, a white X-ray beam is produced by the deflection of charged particles, either electrons or positrons, by means of a bending magnet or an insertion device, *i.e.*, a wiggler or an undulator, as shown in Figure 4 [67]. A monochromator is used to select a narrow energy range from the broad spectrum. For titanium aluminides, energies in the range of 87 to 120 keV, corresponding to wavelengths of 0.143 to 0.103 Å, and wave numbers of 44.1 to 60.1 Å⁻¹ have been shown to yield good diffraction results for specimens of 5 mm in thickness [51].

Specimens are investigated in transmission geometry (Figure 4), as the high-energy X-rays can penetrate relatively large sample volumes. Due to their small wavelengths, they yield narrow Debye-Scherrer cones according to Bragg's law. Thus, large parts of the diffraction patterns, *i.e.*, the diffraction rings, can be recorded at once with the aid of flat-panel area detectors. The latter provide a high temporal resolution, enabling the performance of real-time *in situ* experiments. Poly- and mono-crystalline materials can be investigated by means of HEXRD, as well as texturized or strained materials. As ideally whole diffraction rings are covered, even single diffraction spots from monocrystalline samples can be detected. For conventional powder diffraction purposes, the rings are azimuthally integrated, while anisotropic, directionally-dependent properties can be studied by limiting the integration to segments of the azimuthal angle [68]. Basic aspects and common sources of error in the powder diffraction approach are discussed in [69]. For detailed information on features specific to data collection from neutron and synchrotron radiation sources, the reader is referred to [70].

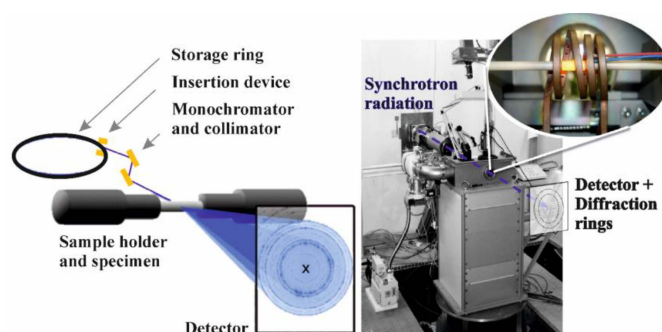


Figure 4. Typical experimental setup for HEXRD. The scheme to the left illustrates the pathway of high-energy X-rays (blue) from their generation at an insertion device in the storage ring, up to their diffraction from the specimen in the sample holder. An area detector at the front captures sets of Debye-Scherrer rings [52]. The photograph on the right shows the quenching and deformation dilatometer [64,66] as an example of a versatile sample environment installed at the PETRA III High Energy Materials Science (HEMS) beamline. In the insert at the top, a heated specimen is glowing during an *in situ* experiment. (Reproduced with permissions from Reference [52]. Copyright © Wiley-VCH Verlag GmbH & Co. KGaA, Weinheim, Germany, 2011).

For *in situ* diffraction experiments, specific conditions concerning temperature, pressure and atmosphere must be adjusted at the sample position. For this purpose, a variety of sample holders and furnaces is currently available. For a large part of the HEXRD experiments presented in this review, a quenching and deformation dilatometer supplied by Bähr Thermoanalyse GmbH, Germany (now TA Instruments), with built-in windows for the X-ray beam, was used (see the photograph in Figure 4) [64]. In this setup, thermal expansion curves and diffraction patterns can be measured simultaneously. Furthermore, thermo-mechanical processing and heat treatments on specimens can be investigated in an *in situ* manner. The dilatometer setup is currently available for high-energy X-rays at the HZG-operated High Energy Materials Science (HEMS) beamline (P07) at PETRA III at DESY in Hamburg, Germany [66]. In the near future, a dilatometer will also be available for neutron scattering at the Heinz Maier-Leibnitz Zentrum (MLZ) in Garching, Germany.

3.2. Studies of Phase Evolutions in TNM Alloys

Knowledge of phase fraction evolutions as a function of temperature and time has adopted a key role in the design and further development of advanced materials. It can be applied to evaluate an alloy's potential regarding future processing routes and applications. The alloy's chemical composition can be optimized as its influence on phase fractions, transition temperatures and kinetics is analyzed. The accuracy of predicted phase diagrams can be verified. If necessary, thermodynamic databases can be modified on the basis of experiments and thermodynamic models improved. Process- and application-related questions can be addressed, treating, for example, the alloy's deformation behavior or its response to heat treatments.

In situ diffraction techniques provide a valuable tool to collect pieces of this fundamental information. Shull *et al.* [46] conducted high-temperature X-ray diffraction experiments on TiAl alloys for phase identification at elevated temperatures. The equipment used comprised a θ - 2θ diffractometer and a linear position-sensitive proportional counter. Specimens were heated in a furnace chamber. The *in situ* experiments proved the presence of the eutectoid reaction for a Ti-45Al (at. %) alloy and allowed the investigation of the $\alpha + \gamma$ phase field region. Novoselova *et al.* [48] applied synchrotron X-ray diffraction to a Ti-46Al-1.9Cr-3Nb (at. %) alloy using a two-circle high-resolution powder diffractometer and an X-ray energy of approximately 9.55 keV. Samples were heated in steps to temperatures ranging from 20 to 1450 °C. Diffraction patterns were acquired under isothermal conditions. In this way, phase fraction evolutions as a function of temperature could be derived in

amounts of Nb or Mo, respectively [74]. Phase fraction evolutions were evaluated by means of quantitative Rietveld analysis. The diffraction experiments were performed at the beamline ID-15B at the European Synchrotron Radiation Facility (ESRF) in Grenoble, France. The samples were slowly heated in a temperature range of 1100 to 1400 °C. DSC measurements and quantitative metallography were performed as complementary characterization techniques. The evolution of the experimentally-acquired phase fractions clearly shows that increased amounts of Nb and Mo shift the β/β_0 minimum at elevated temperatures, which is a characteristic of TNM alloys (Figure 5), to larger phase fractions [74]. A comparison with *ex situ* experiments, however, indicates that the quantitative amount of the β phase at its minimum might be overestimated by the results of the HEXRD experiments on the two modified TNM alloy variants. The heating rate during the *in situ* experiments was chosen as a compromise between limited beam time, avoidance of grain coarsening and time for the achievement of thermodynamic equilibrium conditions. It might have been too high to fully reach thermodynamic equilibrium, especially as the β phase, stabilized by slowly diffusing elements Nb and Mo, exhibits a prolonged dissolution behavior. Nevertheless, Schloffer *et al.* [75] showed that phase fractions retrieved from light-optical microscopy, conventional XRD and *in situ* HEXRD are in good agreement, at least up to the dissolution temperature of the γ phase ($T_{\gamma,solv}$).

3.3. Neutron Diffraction Studies on Order/Disorder Transformations in TNM Alloys

Ordering phenomena strongly affect the mechanical behavior of the phases present in a material and, thus, the mechanical properties of the material as a whole. In TiAl alloys, for instance, the disordered β phase is known to improve hot workability at elevated temperatures [26,76,77], while the ordered β_0 phase has a negative impact on ductility at ambient temperature [78], as well as on creep strength at service temperature [29]. Consequently, the experimental determination of ordering temperatures is of great interest. Using laboratory X-ray sources, *ex situ* studies have been conducted to investigate the site occupancy within different ordered phases [54,79,80]. Complementary investigations of the ordering behavior were conducted by means of TEM [45]. HEXRD experiments were performed to investigate, for example, the site occupancy within the α/α_2 phase in a Ti–45Al–7.5Nb–0.5C (at. %) alloy [81]. A sudden rearrangement of the atomic site occupancies provided evidence for the disordering temperature of the α_2 phase.

Due to short diffusion pathways, ordering reactions are characterized by extremely fast kinetics. The preservation of the disordered states of the α and β phase to room temperature is, thus, impeded, even if the specimens are water-quenched [45,82]. Consequently, the ordering behavior of TiAl alloys can only be investigated at those temperatures, at which the ordering reactions occur, *i.e.*, in an *in situ* manner.

As explained in Section 2, neutron diffraction offers particular benefits regarding the investigation of ordering transitions in TiAl alloys. Hence, the $\alpha \leftrightarrow \alpha_2$ and $\beta \leftrightarrow \beta_0$ ordering/disordering temperatures in a TNM alloy (termed T_{eu} and $T_{\beta,ord}$ in the Ti–Al system) were examined at the structure powder diffractometer SPODI [83,84] at the neutron source FRM II at the MLZ [85]. Specimens were heated in steps ranging from 1000 °C to 1450 °C. Isothermal segments of 3 h allowed the acquisition of diffraction patterns at selected temperatures (Figure 6). Due to the system's peculiarity regarding structure factor considerations, all peaks in the patterns represent superstructure reflections. The Nb-(110) peak, which is indicated in grey, stems from the sample holder.

At temperatures ranging from room temperature to 1100 °C, superstructure reflections of all three phases (α_2 , β_0 and γ) are visible. All phases are present in their ordered state. At 1200 °C, the α_2 reflections have vanished, the α_2 phase has disordered. The transition temperature T_{eu} must therefore lie in the temperature range between 1100 and 1200 °C. Between 1200 and 1250 °C, the $\beta_0 \leftrightarrow \beta$ ordering reaction takes place, the β_0 reflections vanish. Only γ superstructure peaks can be observed at 1250 °C. At 1275 °C, also the γ reflections have disappeared. As the γ phase does not disorder, the disappearance of its superstructure reflections implies its dissolution at $T_{\gamma,solv}$. Thus, at 1275 °C, the

material consists of the disordered phases α and β , as earlier work has proven for temperatures above 1300 °C [23].

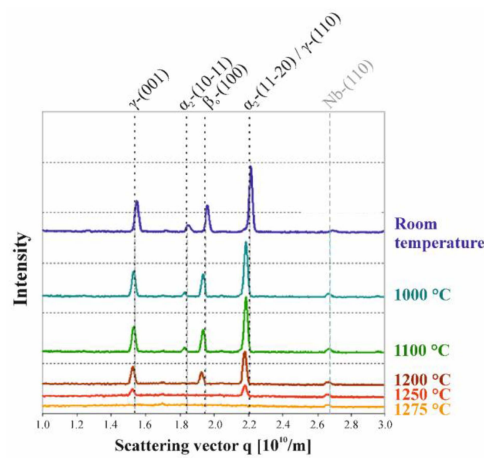


Figure 6. Neutron diffraction patterns of a TNM alloy obtained during isothermal segments at selected temperatures [85]. Between 1100 and 1200 °C, the α_2 reflections vanish, while the β_o phase disorders between 1200 and 1250 °C. The γ phase, which shows no disordering, dissolves in the temperature range between 1250 and 1275 °C.

Due to the extensive pattern acquisition times at SPODI, only a few datasets could be generated. These sets could be used for a rough determination of the temperature ranges in which the order transitions of the α/α_2 and β/β_o phases occur. For a more accurate determination of the ordering/disordering temperatures, neutron diffraction experiments were performed at WOMBAT at the OPAL reactor of the Australian Nuclear Science and Technology Organization (ANSTO) in Lucas Heights, Australia [74,86]. The facility hosts a two-dimensional position-sensitive detector, which is optimized for high-intensity rather than high-resolution measurements and, thus, permits fast data acquisition rates. At heating/cooling rates of $0.166 \text{ K} \cdot \text{s}^{-1}$, the temperatures at which order transitions occur could be determined accurately [74]. An extract of the results obtained in the course of the heating experiments is given in Figure 7. Normalized intensities of the α_2 -(10-11) and β_o -(100) superstructure peaks are presented as a function of temperature. The sharp decrease in intensity indicates the loss of order at relatively fast disordering kinetics. For nominal TNM alloys, T_{eu} was determined to lie at 1174 °C, while $T_{\beta_o,ord}$ was located at 1225 °C [74]. These findings are in perfect agreement with the results obtained previously at SPODI [85].

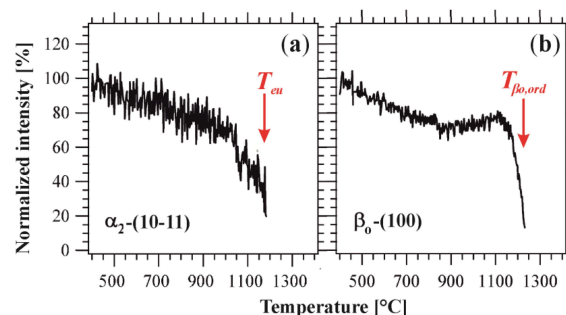


Figure 7. Intensity evolutions of the α_2 -(10-11) (a) and β_o -(100) (b) superstructure peaks during heating. The loss of order is indicated through the sharp decrease in intensity. The intensities, which are plotted as a function of temperature, are normalized to the intensity observed at 400 °C and given in %. (Reproduced with permissions from Reference [52]. Copyright © Wiley-VCH Verlag GmbH & Co. KGaA, Weinheim, Germany, 2011).

For the sake of completeness, it should be noted that with an increasing brilliance of today's synchrotron radiation sources, ordering and disordering reactions in TiAl alloys can also be studied by means of *in situ* HEXRD experiments. Due to the structure factor, however, the intensities of superstructure reflections are generally very weak [87].

3.4. Recent Advancements in the Alloy Development: The Introduction of Carbon to TNM Alloys

The increasing demand for lightweight high-temperature construction materials, higher efficiency and better performance has sparked the need for even more creep-resistant γ -TiAl-based alloys. To meet the requirements, advanced TNM alloys are developed that exhibit good creep resistance and a stable microstructure well above the usual application limit of about 750 °C [38,39].

An increase in creep resistance has often been linked primarily to improvements in the chemical composition of an alloy [10–12,21]. For γ -TiAl-based alloys, a positive effect on creep properties has been reported for the addition of β -stabilizing substitutional solid solution hardening elements (e.g., Nb, Mo, Ta, W), as well as for the addition of interstitial hardening elements (e.g., C, N), which can also form carbides and nitrides. In high Nb- and Mo-containing alloys, solid solution hardening has been shown to be a dominating hardening effect in the γ -TiAl phase. Furthermore, the alloying elements Nb and Mo have been shown to reduce diffusivity and retard thermally-activated dislocation climb during creep [88]. Below their solubility limit, a solid solution hardening effect is also attributed to additions of C and N, albeit these elements are solved interstitially [40,41,89]. Carbon, in particular, has been suggested to impede the growth of α grains due to segregation and to decrease the rate of diffusion in the α phase in cast γ -TiAl-based alloys [21]. Concerning mechanical properties, additions of C and N were found to increase the yield and fracture stresses by the mechanisms of grain refinement, solid solution and precipitation hardening [90]. Especially the precipitation of fine carbides has been shown to considerably increase the high-temperature strength of TiAl alloys [91]. Cubic perovskite Ti_3AlC (*p*-type) carbides have been reported to enhance strength and creep performance for a variety of γ -TiAl-based alloys [10,12,44,91–94]. Hexagonal Ti_2AlC (*h*-type) carbides, on the contrary, are thermodynamically stable at higher temperatures, but are known to be less efficient regarding the impediment of dislocation mobility [10,91]. However, they can act as efficient grain refiners during solidification, yielding a nearly texture-free solidification microstructure, as reported in [38].

Generally, an increase in creep resistance is linked to a decrease in dislocation mobility. However, at room temperature, the ductility of a material may be lost. Therefore, in the course of alloy development, ways of adjusting balanced mechanical properties have to be established. Furthermore, the interplay between different alloying effects has to be considered. Carbon acts as a strong stabilizer of the hexagonally-close-packed α phase and significantly increases the eutectoid temperature T_{eu} . To preserve the solidification pathway via the β phase, the amount of β -stabilizing elements, such as Nb and Mo, has to be corrected, *i.e.*, slightly increased [38]. Thus, grain refinement, minimum segregation and almost texture-free solidification microstructures can still be obtained in C-containing TNM alloys. In this regard, *in situ* diffraction techniques offer a valuable tool to investigate the influence of alloying additions on the solidification behavior of a material, the phase fractions present, as well as their evolution as a function of temperature and time, as reported in [38].

For the investigation of the influence of C additions on the phase evolution in TNM alloys, TNM variants containing 0, 0.25, 0.5, 0.75 and 1 at. % C, respectively, were produced by melting, hot isostatic pressing (HIP), near-conventional forging and subsequent heat treatments [38]. *In situ* HEXRD experiments were conducted at the HZG beamline HARWI II at DORIS III in Hamburg, Germany. Specimens of 5 mm in diameter and 10 mm in length were heated in a modified quenching and deformation dilatometer (Section 3.1; Figure 4). First, the specimens were heated rapidly to 1100 °C. An isothermal segment of 10 min allowed the approach of conditions near thermodynamic equilibrium. Afterwards, the specimens were heated to 1300 °C at a slow heating rate of 2 K·min⁻¹. From 1300 °C to 1425 °C, they were heated at higher rates again to avoid excessive grain growth, which would result in poor grain statistics and the risk of thermocouple tear-off.

The data on the phase fractions as a function of temperature, combined with the results from SEM, were used to derive the quasi-binary phase diagram given in Figure 8 [38]. TNM alloys with a C content below roughly 0.5 at. % still solidify via the β phase (*i.e.*, $L \rightarrow L + \beta \rightarrow \beta \rightarrow \beta + \alpha \rightarrow \dots$), as is known from standard TNM alloys. Thus, intrinsic grain refinement occurs, which stems from the $\beta \rightarrow \alpha$ phase transformation according to the Burgers orientation relationship. Increasing C content entails a change of the solidification pathway from β to peritectic solidification (*i.e.*, $L \rightarrow L + \beta \rightarrow L + \beta + \alpha \rightarrow \beta + \alpha \rightarrow \dots$), as can be observed in the TNM alloys with C contents of 0.5 at. % and above. The peritectic solidification leads to a coarse-grained columnar microstructure with a sharp solidification texture. In the TNM-1C alloy, however, a grain-refining effect was reported to occur due to the formation of *h*-type carbides, which lead to enhanced heterogeneous nucleation during subsequent solid-state phase transformations [38]. Although peritectically solidified, TNM-1C alloys exhibit a fine-grained and texture-free microstructure.

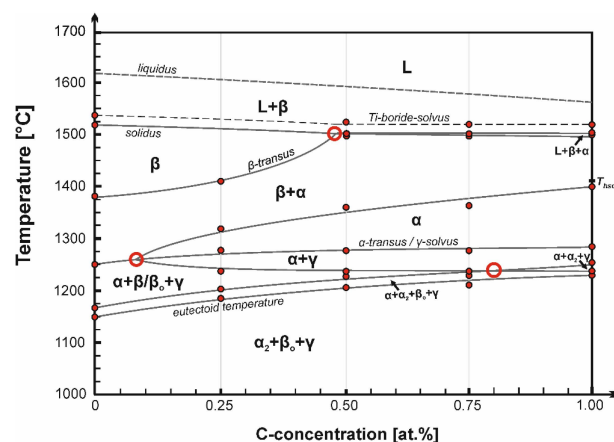


Figure 8. Experimentally-determined quasi-binary section of the TNM-(0–1)C (at. %) system. Evidently, C acts as a strong α stabilizer [38]. (Reprinted from Reference [38], Copyright (2014), with permission from Elsevier).

3.5. Small-Angle Scattering Experiments on Carbide Precipitation in TNM Alloys

In a forged and heat-treated TNM alloy containing 1 at. % C (in the following termed TNM-1C), Ti_2AlC *h*-type carbides were found (see the previous section), whereas no Ti_3AlC *p*-type carbides could be detected. TEM investigations confirmed the absence of both *h*- and *p*-type carbides within cast/HIP, as well as forged and heat-treated alloy variants containing lower amounts of C. In these alloys, the solubility limit of C may not have been exceeded. In this regard, it has to be noted that the overall composition of the alloys may impact the results concerning the presence and type of carbides. Small-angle neutron scattering (SANS) studies proved the presence of *p*-type precipitates in a Ti–48.5Al–0.4C (at. %) alloy after a solution treatment for 4 h at 1250 °C followed by ageing for 24 h at 750 °C and quenching [42]. As a result of the precipitation-hardening treatment, the material's high-temperature strength was improved. Further SANS experiments, which targeted the effect of an addition of 0.5 at. % C to Ti–45Al–5Nb (at. %) alloys, showed that in contrast to the Nb-free alloys, the Nb-containing alloys exhibit no strengthening precipitates, but rather a homogeneous C distribution with a few C-enriched regions [43]. Investigations on a powder-metallurgically produced TNB alloy, on the other hand, which differs in its Al and Nb content from the TNM specimens and is moreover Mo-free, evidenced the presence of *p*-type carbides at 0.75 at. % C [95]. Recently, Wang *et al.* [96] systematically investigated the nucleation, growth and coarsening of carbides in C-containing Ti–45Al–5Nb (at. %) alloys by means of HEXRD and TEM studies.

Generally, not only the chemical composition, but also the heat treatment history determines if, which type and to what extent carbides are present in a material. In a follow-up study on

a TNM-1C alloy, the precipitation behavior and thermal stability of the Ti_3AlC p -type carbides during isothermal annealing and subsequent re-heating to 1200 °C were quantified [44]. HEXRD experiments were conducted to study the phase transformation and precipitation behavior of the carbides from a supersaturated matrix. Thereby, the matrix was formed by ultrafine γ lamellae, which precipitated themselves during the heat treatment in supersaturated α_2 grains, building up hierarchical structures on the nanoscale. *In situ* small-angle X-ray scattering (SAXS) experiments using synchrotron radiation were conducted to gain a deeper insight into the size distribution, precipitation kinetics and thermal stability of the carbide precipitates.

The SAXS experiments were conducted at the HEMS beamline at PETRA III [44]. In Figure 9, the experimental setup is schematically illustrated. In principle, it resembles closely the HEXRD setup described in Section 3.1. A major difference, however, lies in the fact that the sample-to-detector distance must be larger for SAXS experiments, as the X-rays scattered at small angles are studied with high resolution. As indicated in Figure 9, a second area detector might be positioned in the optical path of the diffracted X-rays to record the HEXRD pattern at times or to record part of the diffraction rings simultaneously to the *in situ* SAXS experiment.

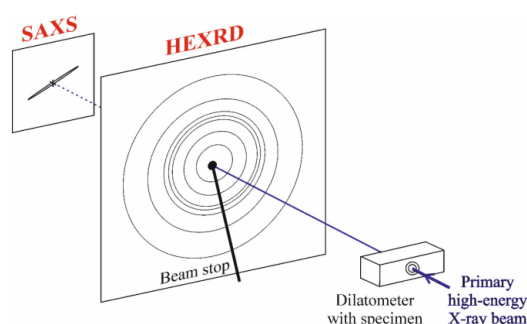


Figure 9. Schematic of the experimental setup for SAXS experiments conducted on C-containing TNM alloy variants [44]. The primary X-ray beam impinges on the specimen within the dilatometer (see Figure 4) and is subsequently scattered/diffracted. Two-dimensional detectors record the SAXS (and if desired, the HEXRD) signal.

For the *in situ* investigation of the carbide precipitation behavior in the TNM-1C alloy, cylindrical specimens of 5 mm in diameter and 10 mm in length were inductively heated in an adapted quenching and deformation dilatometer (Section 3.1; Figure 4). The recorded diffraction patterns were azimuthally integrated using the software program Fit2D [97]. The derived scattering curves were fit within SANSFit based on a least-squares method iteration, as conducted in [42]. The p -type carbides were modelled as elongated ellipsoids of revolution. A random orientation of particles was suggested, obeying a lognormal size distribution.

Figure 10 illustrates the time-temperature profile of the conducted heat treatment. The first annealing step, which consisted of an isothermal segment of 1 h in the $(\alpha + \beta)$ phase field region at 1415 °C followed by quenching, was performed *ex situ* in a high-temperature furnace to avoid thermocouple tear-off. The resulting microstructure at room temperature consisted primarily of supersaturated α_2 grains, as well as a small amount of ordered β_0 phase that additionally contained martensitic α_2' . The subsequent isothermal stabilization or precipitation annealing and the ensuing re-heating were conducted in the dilatometer in the optical path of the synchrotron beam, while the SAXS and HEXRD signals were continuously recorded. Regarding the microstructure, the isothermal annealing at 750 °C for 4 h provoked the transformation of the supersaturated α_2 grains to lamellar α_2/γ colonies as γ lamellae precipitated obeying the Blackburn orientation relationship [98]. Furthermore, lens-shaped γ particles precipitated within β_0 according to a modified Kurdjumov-Sachs orientation relationship. P -type Ti_3AlC carbides occurred in the γ phase according to the orientation relationship reported in [91]. The precipitation of p -type carbides was attributed to the low solubility

of C in the γ phase, which was found to be six-times lower than in the α_2 phase, while the β_o phase exhibits in general almost no solubility for C [38,41]. The re-heating of the specimens from 750 to 1200 °C yielded a fine-grained α_2/γ phase arrangement due to the occurrence of discontinuous coarsening (cellular reaction) [99]. As the thermal activation of diffusion processes is enhanced with increasing temperature, the microstructural instability becomes increasingly pronounced. The p -type carbides dissolve in γ as the C solubility increases.

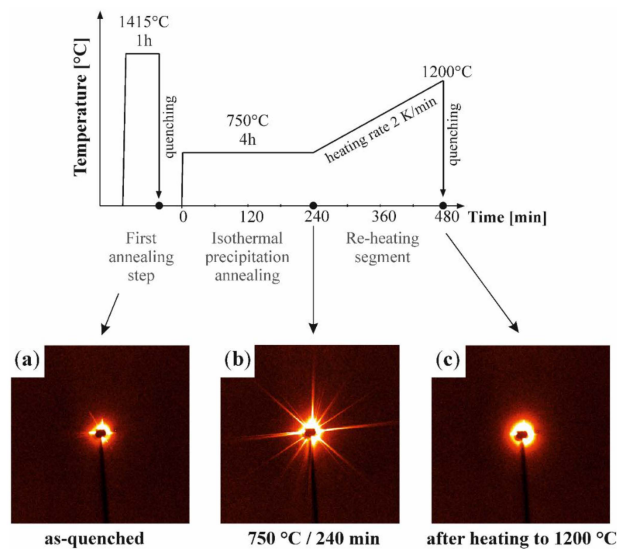


Figure 10. Time-temperature profile of the heat treatment conducted as described in [44]. Dots at certain stages of the profile correspond to the SAXS detector images displayed below (a,b,c). See the text for details.

In Figure 10, SAXS detector images recorded at selected stages during the *in situ* experiment (indicated as dots on the time scale of the heat treatment plot) are shown. In all cases, a pronounced small-angle scattering signal is visible around the beam stop. Figure 10a corresponds to the quenched and supersaturated state after the first annealing step at 1415 °C. Small streaks in the SAXS signal are attributed to the martensitic structure of α_2' in β_o , as described in [44]. During the initial stage of the annealing segment at 750 °C, these streaks vanish. After an incubation time of roughly 30 min, however, new streaks can be observed. Appearing more pronounced, they are assigned to smaller structural features within the hierarchical structure. Furthermore, the incubation time for nucleation indicates that the streaking does not stem from ultrafine γ lamellae, which form directly after thermal activation at 720 °C, but rather from the p -type carbides precipitating in γ -laths. Figure 10b shows the SAXS signal at the end of the isothermal precipitation segment. Heating to 1200 °C leads to the disappearance of the streaks (Figure 10c), which can be attributed to the dissolution of the p -type carbides within the γ -lamellae.

The SAXS detector images were evaluated regarding the carbide precipitation kinetics as well as their thermal stability. In Figure 11, selected averaged scattering curves during isothermal annealing and subsequent heating are shown. The time specifications are given in accordance with the time scale set in Figure 10, *i.e.*, 0 min refers to the beginning of the isothermal segment. The magnitude of the scattering vector q inversely corresponds to the characteristic dimensions (e.g., radii) of the precipitated particles, while the macroscopic scattering cross-section $d\Sigma/d\Omega$ is directly proportional to the fraction and number of p -type carbide precipitations. After a distinct incubation time of roughly 30 min, the scattering curves increase in $d\Sigma/d\Omega$, indicating an increase of the precipitate volume fractions. After 333 min, the specimen has already entered the heating segment (at a temperature of 936 °C), and an inverse trend begins to manifest itself. This means that the p -type carbides begin to dissolve, provoked by the increasing temperature (see the time-temperature profile in Figure 10).

From the scattering curves, the number density, volume fraction and characteristic dimensions of the precipitates can be estimated [44].

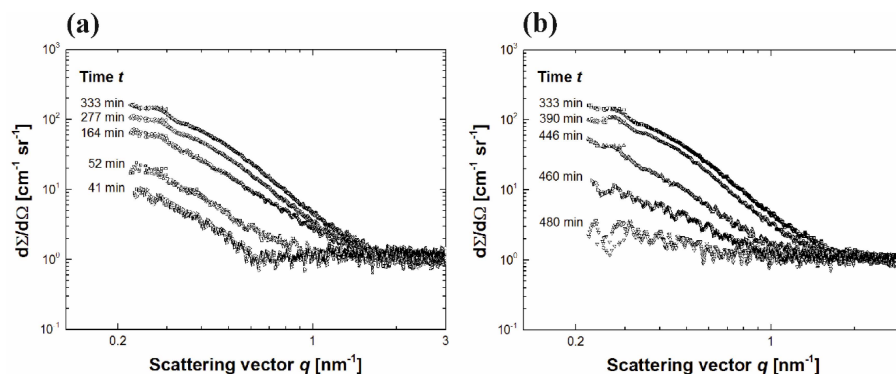


Figure 11. Selected averaged scattering curves during isothermal annealing and subsequent heating. Until 333 min (936 °C), p -type carbides precipitate in the γ laths of the α_2/γ colonies (a). Afterwards, their volume fraction decreases again (b). The indicated time specifications refer to the time scale set in the time-temperature profile depicted in Figure 10. (Reprinted from Reference [44], Copyright (2014), with permission from Elsevier).

4. TNM Alloys during Processing at Elevated Temperatures

4.1. General Considerations on the Mapping of Deformation, Recovery and Recrystallization

For the investigation of the structure and structural changes in crystalline materials, a multitude of methods based on X-ray diffraction exists. Conventional powder diffraction methods that average over many crystallites offer information on lattice parameters, phase fractions, texture and internal stresses. If monochromatic radiation is used, a fine-grained and homogeneous material will yield a diffraction pattern related to the intersection of the detector (point, line or plane) with the created Debye-Scherrer cones. In transmission geometry, Debye-Scherrer rings will, for example, appear on an area detector. If a monochromatic beam impinges only on a small number of crystallites, be it due to a small beam cross-section or due to a coarse-grained microstructure, information on individual crystallites can be extracted from the resulting reflection spots, which sit on the according positions on the Debye-Scherrer rings [77]. In this regard, three-dimensional X-ray diffraction microscopy (3DXRD) has emerged as a powerful technique enabling the tracking of reflections of individual grains over time [100–103]. Depending on the selected setup, nucleation and growth studies, grain-by-grain volumetric mapping or orientation imaging microscopy can be performed to study undeformed or deformed material regarding recrystallization, grain growth and grain orientations.

Alternatively, if only a few grains are illuminated, white-beam Laue diffraction can be applied. The result is a Laue pattern characteristic of the crystal lattice and its orientation with respect to the incident beam. A typical field of application of the white-beam Laue technique is the adjustment of the orientation of TiAl single crystals as performed by Inui *et al.* [104]. The advantage of this method lies in the fact that reflections of the lattice planes stay visible in the Laue pattern if the crystal is rotated about an arbitrary axis. Using a monochromatic beam, only lattice planes in the diffraction condition are visible [101]. Consequently, the Laue technique is well suited for the investigation of the deformation and recrystallization behavior of single crystals [105,106]. However, it is less advantageous for the investigation of fine-grained polycrystalline samples. In these samples a large number of grains is illuminated at once, resulting in complex Laue patterns that are difficult to evaluate.

In these cases, it may be favorable to conduct HEXRD experiments using monochromatic X-rays (Section 3.1; Figure 4). To study recovery, recrystallization and grain growth processes, the intensity distribution of one or more Debye-Scherrer rings can be evaluated as a function of time. If a large

number of grains is illuminated by the incident beam, information concerning texture [107] and strain can be derived from the inhomogeneity along the Debye-Scherrer rings. If reflections from single grains can be distinguished, the patterns can be evaluated regarding a variety of additional parameters, such as the number of spots, their morphology, their arrangement and their evolution with time [50]. Information regarding grain sizes, grain refinement or coarsening, mosaic spread and grain orientations can be retrieved. In terms of heat treatments, for instance, the rearrangement of differently-oriented grains in a massively-transformed TiAl sample has been studied upon heating [82,108]. Careful analysis of single diffraction patterns even allowed tracing the phase transformations of single grains, as diffuse streaking between the parent and the newly-formed grains was observed in a TiAl alloy, as reported in [109]. Individual reflection spots might also transform characteristically during an experiment emulating, for example, hot deformation. A simplified model of the development of reflection spots during hot working is proposed in [52]. The way in which the diffraction pattern is affected depends on the processes dominating in the material, e.g., whether a material or phase predominantly shows recovery or rather recrystallization under the conditions applied. The evaluation of diffraction patterns can help to distinguish these processes and to characterize the evolution of polycrystalline materials undergoing thermo-mechanical processing.

An intuitive approach to visualize the evolution of reflection spots pertaining to one crystallographic plane is to plot the diffracted intensity along the azimuthal angle of a specific ring as a function of time (azimuthal angle *vs.* time (AT) plot) [50]. For this plot, an integration over a small Bragg-angle range has to be performed, which includes only the Debye-Scherrer ring of interest. Yan *et al.* [110] used this form of data representation to illustrate the formation of texture during the deformation of an initially coarse-grained Cu sample. In a similar experimental setup, recovery and recrystallization processes were studied in a Zr alloy during hot compression [111]. Mosaicity was derived from the azimuthal angle spread of single reflection spots. The formation of subgrains was studied as single spots of large angular spread split into many sharp reflections separated by small angles. Recrystallization was identified at a later stage of the experiment by the rapid appearance or disappearance of reflection spots.

4.2. HEXRD Studies on the Hot Deformation Behavior of TNM Alloys

The approach of creating AT plots (Section 4.1) was adopted to study the hot deformation behavior of a TNM alloy [112]. HEXRD experiments were conducted at the ID15 beamline at ESRF. Cylindrical specimens of 4 mm in diameter and 8 mm in length were heated resistively to 1300 °C between the anvils of an electro-thermo-mechanical tester supplied by Instron, Norwood, USA, and subsequently compressed. In Figure 12, the AT plots of two selected Debye-Scherrer rings are given. Figure 12a illustrates the evolution of the α_2/α -(20-21) ring, Figure 12b the one of β_0/β -(002). In Figure 12c, the temperature profile, as well as true stress and true strain curves are given as a function of time.

At the beginning of the experiment, the evolution of the individual reflection spots over time results in distinct lines in the AT plots, which are in the following referred to as timelines. For both phases, α_2/α and β_0/β , continuous timelines are observed during heating. While the specimen is held at 1300 °C within the ($\alpha + \beta$) phase field region, the α reflections remain steady, while the β phase reflections fluctuate. Upon the onset of deformation, the intensity distribution immediately changes for both phases. Concerning the α phase, diverting, yet continuous timelines are discernible, which exhibit a blurred appearance. The β phase reflections, on the other hand, broaden partly and become sharp spots. After 215 s, the sample was unloaded for 30 s to investigate the material's response. Upon this, the α phase timelines remain again continuous, but blurred, while the β phase reflections fluctuate fast and yield sharp timelines.

The inserts in the respective figures highlight the material's behavior from the start of deformation up to the end of the interim unloading period. Diverted timelines stem from the rotation of a crystal lattice of a grain about an axis parallel to the incident beam. In contrast to this, the broadening of a reflection indicates an increasing defect density within the grain [113]. Sharp dots, which relate to

one original reflection and occur within a small angular range, are caused by subgrains stemming from a dynamic recovery process [77,111]. As peak broadening followed by the formation of new reflection spots can be observed in the insert of Figure 12b, fast dynamic recovery processes are suggested to dominate the β phase. In the α phase, however, the reflections are diverted around small azimuthal angles and appear blurred, indicating the deformation by dislocation slip and the presence of high defect densities. The absence of reflections with low angular spread points to slow recovery processes instead of discontinuous recrystallization processes [77]. For the validation of the results of the presented *in situ* HEXRD experiment, electron-backscatter diffraction (EBSD) measurements were performed on the deformed specimens. These investigations, which are elaborately described in [52,112], have confirmed the results derived from the *in situ* experiments. No indication of appreciable dynamic recrystallization was found for both phases α/α_2 and β/β_0 .

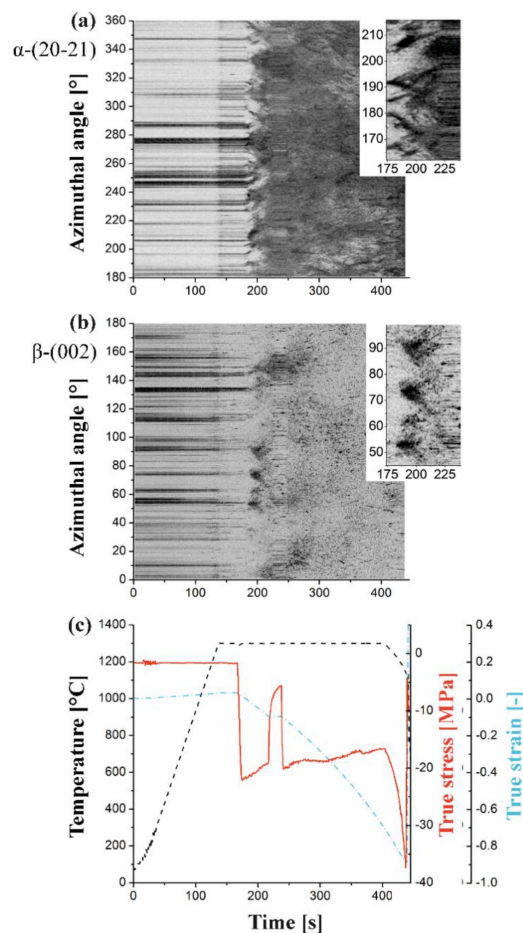


Figure 12. Azimuthal angle *vs.* time (AT) plots of the α_2/α -(20-21) (a) and the β_0/β -(002) reflections (b) illustrating the hot deformation behavior of a TNM alloy. The temperature profile, true stress and true strain are given as a function of time (c). The *in situ* deformation experiment was conducted within the ($\alpha + \beta$) phase field region [112]. (Reproduced with permissions from Reference [52]. Copyright © Wiley-VCH Verlag GmbH & Co. KGaA, Weinheim, Germany, 2011).

In situ HEXRD experiments during deformation were also conducted on TNM alloys containing minor additions of C and Si [114]. For this purpose, the deformation unit of the quenching and deformation dilatometer (Section 3.1) was used at the HZG beamline HARWI II at DESY. Phase fraction and texture evolutions, as well as temperature uncertainties arising during compression, were studied. The information retrieved complemented uniaxial compressive hot-deformation tests performed on

a Gleeble 3500 simulator at temperatures ranging from 1150 to 1300 °C and strains rates between 0.005 and 0.5 s⁻¹.

5. Heat Treatments for Balanced Mechanical Properties

5.1. Microstructural Evolution: The Formation of Lamellar α_2/γ Colonies in a TNM Alloy

For the adjustment of optimized properties, the control over the phases present in a material, specifically in terms of composition, volume fraction and arrangement, is indispensable. Processes taking place during phase transformations, such as the precipitation or dissolution of phases, offer opportunities for targeted manipulation. Knowledge of these transformations is, thus, of great technological importance. Comprehensive insight into the prevailing processes can be gained, for example, by taking a two-fold approach. While *in situ* diffraction and scattering techniques offer information on the evolution of phase fractions and kinetic aspects, complementary *in situ* or *ex situ* studies of the microstructure (e.g., by means of SEM or TEM) unveil the arrangement of the various phases in real space.

In TiAl alloys, mechanical properties strongly depend on the occurrence and structure of lamellar α_2/γ colonies [31,32,115,116]. For this reason, the $\alpha \rightarrow \alpha_2/\gamma$ transformation has been the subject of thorough investigation, both from technological and scientific points of view [4,48,52,109,117–119]. In TiAl alloys, the γ phase dissolves upon heating at $T_{\gamma, solv}$. Depending on the chemical composition, the alloy then enters the ($\alpha + \beta$) or the single α phase field region (Figure 5). If the specimen is again cooled down from this phase field region, γ lamellae tend to form within supersaturating α grains [5,118,120]. The cooling rate has been proven to be a decisive parameter for the lamellar spacing within the forming α_2/γ colonies [118,121]. However, if the alloy is cooled at a sufficiently high rate, the microstructure present at elevated temperatures is roughly preserved, and the formation of the γ phase is suppressed. Ordering reactions take place, but the α_2 grains remain in a supersaturated state. In the course of a subsequent heat treatment, (ultra)fine γ lamellae can precipitate in the supersaturated α_2 grains [28,109,122,123]. In this case, the lamellar spacing strongly depends on the temperature profile during the heat treatment, *i.e.*, the heating rate and maximum temperature during continuous heating or the holding temperature in isothermal heat treatments [116,124]. The formation of fine γ lamellae improves the mechanical properties of a material in terms of strength, plastic fracture strain, fracture toughness and creep resistance at service temperature [5,10,11,53,116,120,122,125].

To study the onset of the γ lamellae precipitation in the course of continuous heating in a Ti–45Al–7.5Nb (at. %) alloy, *in situ* experiments were conducted at the beamline ID15A/B at the ESRF [109]. A two-dimensional detector enabled the investigation of diffuse and inter-Bragg peak scattering. The reflections recorded in reciprocal space were observed to form streaks, which correlated with the precipitation and formation of ultrafine γ lamellae. High temperature laser scanning confocal microscopy was used as a complementary technique to verify the obtained results [109]. *In situ* TEM studies of the initial stages of lamellae formation in a Ti–45Al–7.5Nb (at. %) alloy were performed by Cha *et al.* [126]. During heating, γ laths were found to precipitate at roughly 750 °C according to the Blackburn relationship [98], following the formation and motion of dislocations next to interfaces at 730 °C. As *in situ* TEM, however, comprises many experimental difficulties, the majority of reported TEM studies is restricted to *ex situ* characterizations. Nevertheless, valuable data on lamellae thickness and spacing can be obtained, which are generally not accessible by means of other characterization methods.

To investigate the precipitation of γ lamellae in TNM alloys, specimens were subjected to a two-step heat treatment (Figure 13) while being simultaneously probed by means of HEXRD [52]. The first step in the heat treatment was designed to create supersaturated α_2 grains through rapid quenching from 1230 °C. The second heat treatment step consisted of a continuous heating ramp, during which fine γ lamellae precipitated in the α_2 grains [28,72]. In Figure 13a, the temperature profile of the heat treatment is shown superimposed by the intensity evolution of the γ -(200) peak,

which was evaluated by fitting a Gaussian to the relevant q -range of the azimuthally-integrated diffraction patterns. The rapid heating of the specimen during the first heat treatment step results in a decreasing peak intensity, indicating a strong decrease in the amount of γ phase with increasing temperature. During the isothermal segment at 1230 °C, the γ phase fraction further decreases as the phase approaches thermodynamic equilibrium. After 300 s, the specimen is quenched to room temperature. Upon this, an increase in peak intensity is observed, indicating a small increase in the amount of γ phase. The precipitation and growth of the γ phase has not completely been suppressed. However, the hindrance was sufficient to create supersaturated α_2 grains, which contain only a few γ lamellae (Figure 13b, top). After quenching, the specimen is continuously heated at a low heating rate. Until about 765 °C, no major changes are observed in the peak intensity evolution. At temperatures well above 865 °C, however, the γ phase fraction increases rapidly. This increase is attributed to the precipitation of fine γ lamellae (Figure 13b, bottom). *Ex situ* TEM studies performed by Cha *et al.* [115,116] document that an average interface spacing in the range of 5 to 40 nm can be adjusted in heat-treated TiAl alloys.

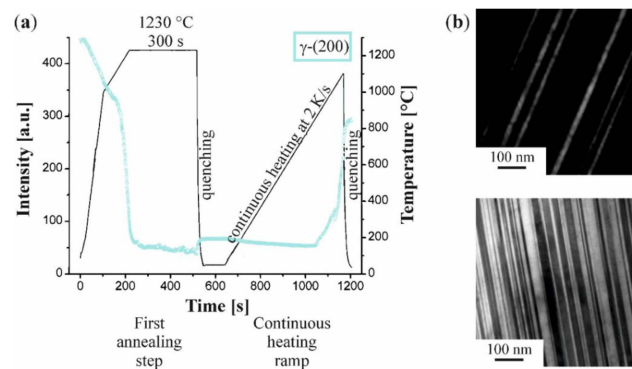


Figure 13. Temperature profile applied during the heat treatment of a TNM alloy, shown superimposed by the intensity evolution of the γ -(200) peak (blue) (a). The heat treatment was conducted in two steps and resulted in the precipitation of fine γ lamellae. Exemplary TEM images show the presence of only few γ lamellae in the supersaturated α_2 grains after quenching (b, top). After annealing, the number and volume fraction of fine γ lamellae has significantly increased (b, bottom). (Reproduced with permissions from Reference [52]. Copyright © Wiley-VCH Verlag GmbH & Co. KGaA, Weinheim, Germany, 2011).

5.2. Studies Enabling the Targeted Optimization of Heat Treatment Steps

In TNM alloys, heat treatments must be applied after hot deformation as high amounts of the ordered β_0 phase would deteriorate the material's properties at room and service temperature [11,20,25,29,127]. Adapted post-forging heat treatments have been reported in [20,28,29,115,116,128–130]. These heat treatments typically comprise three steps [131]. In the first heat treatment step, the material is homogenized as reported in [129]. Subsequently, a high-temperature annealing step is conducted either in the $(\alpha + \beta + \gamma)$ or in the $(\alpha + \beta)$ phase field region. The aim is the minimization of the β phase fraction, the setting of the volume fraction of globular γ grains and the adjustment of the size of α grains, which act as precursors of the lamellar α_2/γ colonies. The third annealing step represents a stabilization treatment near 900 °C and is followed by furnace cooling. According to the Blackburn orientation relationship [98], γ lamellae precipitate in supersaturated α_2 grains or α_2/γ colonies (Section 5.1), causing an increase in hardness. The lamellar spacing within the colonies is usually attempted to be kept small to gain a substantial increase in strength through a modified Hall-Petch relationship [115,116]. For detailed information regarding the mechanical properties of TNM alloys, the reader is referred to [11,28,37,114]. In ultrafine lamellae, however, the driving force for discontinuous coarsening (cellular reaction) is greatly increased, which has

a negative impact on the material's creep properties [39,99,132]. Processing parameters, such as annealing temperatures or heating and cooling rates, have to be carefully selected to obtain balanced properties [115,133,134].

As the mechanical properties of TNM alloys are determined by the precipitation of γ lamellae during the third annealing step, the adjustment of a favorable starting condition during the second heat treatment step, *i.e.*, supersaturated α_2 grains for a maximum driving force in γ precipitation, is of great importance. The microstructural evolution upon cooling has been thoroughly studied in several γ -TiAl-based alloys [109,118,133,135–139]. The influence of varying cooling rates on the grain size and the appearance of lamellar structures in particular was studied and linked to the resulting mechanical properties. The applied methods included short- and long-term heat treatments combined with metallography, dilatometry, differential scanning calorimetry, micro-hardness testing and TEM. Diffraction methods, such as HEXRD, have been used for the investigation of phase fraction evolutions as a function of temperature and time [50,51,65,77,82,128,130].

To investigate the influence of technologically relevant cooling rates on the evolution of the γ phase during the second heat treatment step, a TNM alloy with increased amounts of β -stabilizing alloying elements Nb and Mo was studied by means of *in situ* HEXRD [87]. The diffraction experiments were conducted partly at HARWI II and partly at PETRA III. In a dilatometer setup in the synchrotron beam (Section 3.1; Figure 4), forged and homogenized specimens were annealed for 10 min at 1235 °C in the ($\alpha + \beta + \gamma$) phase field region below the γ -solvus temperature $T_{\gamma,solv}$ and subsequently subjected to linear cooling rates ranging from 35 to 1200 K·min⁻¹. After reaching 600 °C, the specimens were quenched at the highest rate possible. The correlation between the linear cooling rates, the phase fraction evolutions and the resulting microstructures was investigated.

In accordance with [118,133,138], the resulting α/α_2 phase fractions upon cooling were found to increase significantly with increasing cooling rate. At high cooling rates, the time available for diffusion-controlled processes is shorter, and a larger fraction of the untransformed, supersaturated α_2 phase remains. With the aid of the *in situ* HEXRD experiments, the phase fractions could be accurately quantified. Furthermore, the increase in the amount of α/α_2 phase was observed to occur primarily at the expense of the γ phase, whose phase fractions decreased with increasing cooling rate. From these results, a plot analogous to a continuous-cooling-transformation (CCT) diagram was derived (Figure 14), including all investigated cooling rates. In this plot, broad black lines confine regions in which the indicated γ phase fraction is exceeded. Experimental points representing conditions close to thermodynamic equilibrium were obtained from preliminary diffraction experiments [87].

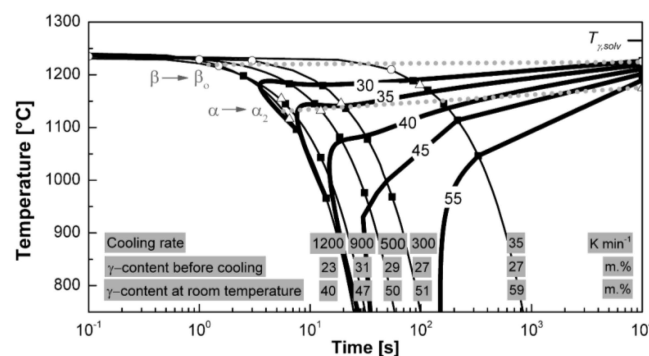


Figure 14. Continuous-cooling-transformation (CCT) diagram for the γ phase precipitation during the heat treatment of a TNM alloy. Broad black lines confine regions in which the given γ phase fraction (in m %) is certainly exceeded. The cooling paths plotted as narrow black lines result from the linear cooling rates of 35, 300, 500, 900 and 1200 K·min⁻¹, respectively. Thus, the influence of technologically relevant cooling rates on the quantitative gain in the γ phase can be derived [87]. Actual γ phase fractions (in m %) before and after cooling are indicated in the boxes at the bottom. (Reprinted from Reference [87], Copyright (2015), with permission from Elsevier).

The temperatures at which specific amounts of γ phase are present decrease in accordance with [135] with increasing cooling rate, while the phenomenon is enhanced for higher cooling rates. The γ phase fractions determined at the end of the isothermal annealing segment, *i.e.*, before cooling and after cooling to room temperature, are given in Figure 14. Comparing the four specimens that were cooled at constant cooling rates in the range of 35 to 900 K·min⁻¹, the quantitative gain in γ phase upon cooling generally decreases as the cooling rate increases. The specimen cooled at 1200 K·min⁻¹ exhibits at room temperature, as expected, the lowest γ phase fraction (40 m %). The quantitative gain in γ phase, however, is slightly elevated when compared to the specimen cooled at 900 K·min⁻¹ (from 31 to 47 m %). This behavior is attributed to the fact that this specimen exhibited with 23 m % the lowest γ phase fraction at the end of the isothermal annealing segment, corresponding to a higher actual annealing temperature. Due to differences in the actual starting temperatures, the gain in γ phase as a quantity is not suitable as an absolute means of comparison. Comparison of the γ phase fractions at room temperature is more reliable.

As all specimens were cooled from the ($\alpha + \beta + \gamma$) phase field region, a certain amount of the γ phase is present in the specimens from the beginning. From Figure 14, it can be concluded that even at cooling rates as high as 1200 K·min⁻¹ further gain in γ phase cannot be suppressed. During cooling, the overall amount of the γ phase increases. At high cooling rates, however, a sufficient amount of supersaturated α/α_2 grains can be obtained, rendering possible the formation of fine lamellar structures in an ensuing annealing step, as described at the beginning of this section. Investigation of the resulting microstructures by means of SEM and TEM offers additional information for the design of a suitable time-temperature profile in the second heat treatment step typical of TNM alloys.

6. Summary

In situ diffraction and scattering techniques based on synchrotron radiation and neutrons offer unique opportunities for the development of advanced structural materials. They enable the exploration of a multitude of aspects, which are usually not accessible with the aid of conventional methods. The present review attempts to shine a light on selected *in situ* diffraction and scattering techniques, highlighting the ways in which they promoted the development of intermetallic TNM alloys based on the γ -TiAl phase.

In situ studies of phase evolutions, as discussed in Section 3, provide answers to fundamental research questions. They reveal phase fractions and transition temperatures and allow to study influencing parameters under controlled experimental conditions. Measurements on several model alloys of differing chemical compositions provide the basis for the establishment of phase diagrams [37]. Furthermore, the specific influence of certain alloying elements can be studied. For instance, it was found that the amount and type of β -stabilizing alloying elements significantly influences the phase evolution character of the β phase, which plays a decisive role in post-forging heat treatments [65]. Diffraction techniques also promoted the development of TNM alloys containing harmonized additions of C and Si, as they enabled the investigation of the influence of the alloying additions on the solidification behavior and phase fraction evolution within the material [38]. SAXS and SANS studies offered insights into the carbide precipitation behavior of these advanced alloys [44]. For the investigation of order/disorder transitions, typically, neutron diffraction experiments are conducted. Due to peculiarities in the structure factors of titanium aluminide alloys (Section 2), they offer distinct advantages. *In situ* studies are again indispensable, as ordering reactions are characterized by extremely fast kinetics. Consequently, the ordering behavior of TiAl alloys can only be investigated at those temperatures at which the ordering reactions occur [65,85].

The second part of the present review exemplarily introduces approaches to processing- and application-related questions. For the investigation of the hot deformation behavior, for example, AT plots can be applied (Section 4). With this technique, an understanding of the processes prevailing in TNM alloys during hot working could be established [112]. After hot deformation, heat treatments are applied to TNM alloys to adjust balanced mechanical properties (Section 5). For this purpose, control

over the phases present in the material, specifically in terms of composition, volume fraction and arrangement, is indispensable. To extend the necessary knowledge bases, the formation of lamellar α_2/γ colonies was investigated from a diffraction point of view and complemented by the results from conventional characterization techniques [52]. Finally, *in situ* HEXRD techniques were used as a tool for the targeted optimization of heat treatments [87].

Continuous progress in hardware development, especially detector technology, as well as the construction of dedicated diffraction beamlines of increasing brilliance provide the necessary base for *in situ* experiments at high frame rates. Simultaneously to this development, new techniques are emerging that comprise valuable tools for a multitude of applications in materials science. Besides HEXRD, neutron diffraction and SAXS/SANS, great potential for future investigations is seen, for example, in nano-beam experiments and in the 3DXRD technique. Diffraction and scattering methods have significantly contributed to the characterization and development of advanced multi-phase γ -TiAl-based alloys during the last 25 years. Undoubtedly, also in the future, characterization techniques based on synchrotron radiation and neutrons will promote the understanding of this class of innovative, lightweight, high-temperature materials.

Acknowledgments: Some of the research studies presented in this review were conducted at the HZG beamlines HARWI II and HEMS at DESY. The support of the DESY management, user office and HZG beamline staff is gratefully acknowledged. In particular, the authors would like to thank Thomas Lippmann, Norbert Schell, Lars Lottermoser, Torben Fischer and René Kirchof for their assistance at the beamlines. Some studies are based on experiments performed at the ESRF and the MLZ. Access and support of the respective managements, user offices and beamline staff are appreciated. The contribution of Kun Yan to the successful realization of the neutron scattering experiments at ANSTO is gratefully acknowledged. Parts of the research pursued by the authors affiliated with the Montanuniversität Leoben received support by the European Commission under the 7th Framework Programme through the “Research Infrastructures” action of the “Capacities” Programme (Contract No. CP-CSA_INFRA-2008-1.1.1 Number 226507-NMI3), by the European Community’s 7th Framework Programme (FP7/2007e2013) under Grant Agreement No. 226716 and by the Styrian Materials Cluster, Austria. Some of the studies were conducted within the frameworks of the German BMBF Project O3X3530A and of the Austrian FFG Project 830381 “fAusT” of the Österreichisches Luftfahrtprogramm TAKE OFF.

Author Contributions: All authors contributed equally to this work. P.E. wrote the bulk of the manuscript in close collaboration with the other authors. The contribution of the authors to the experimental work is specified in the respective original publications cited throughout this work.

Conflicts of Interest: The authors declare no conflict of interest.

References

1. Bewlay, B.P.; Weimer, M.; Kelly, T.; Suzuki, A.; Subramanian, P.R. The science, technology, and implementation of TiAl alloys in commercial aircraft engines. *MRS Proc.* **2013**, *1516*, 49–58. [[CrossRef](#)]
2. Clemens, H.; Smarsly, W.; Güther, V.; Mayer, S. Advanced intermetallic titanium aluminides. In Proceedings of the 13th World Conference on Titanium, San Diego, CA, USA, 16–20 August 2015.
3. Habel, U.; Heutling, F.; Helm, D.; Kunze, C.; Smarsly, W.; Das, G.; Clemens, H. Forged intermetallic γ -TiAl based alloy low pressure turbine blade in geared turbofan. In Proceedings of the 13th World Conference on Titanium, San Diego, CA, USA, 16–20 August 2015.
4. Yamaguchi, M.; Inui, H.; Ito, K. High-temperature structural intermetallics. *Acta Mater.* **2000**, *48*, 307–322. [[CrossRef](#)]
5. Appel, F.; Wagner, R. Microstructure and deformation of two-phase γ -titanium aluminides. *Mater. Sci. Eng. Rep.* **1998**, *R22*, 187–268. [[CrossRef](#)]
6. Kim, Y.-W.; Clemens, H.; Rosenberger, A. *Gamma Titanium Aluminides 2003*; The Minerals, Metals and Materials Society (TMS): Warrendale, PA, USA, 2003.
7. Kim, Y.-W.; Kim, S.; Dimiduk, D.M.; Woodward, C. Development of beta gamma alloys: Opening robust processing and greater application potential for TiAl-base alloys. In *Structural Aluminides for Elevated Temperature Applications*; The Minerals, Metals and Materials Society (TMS): Warrendale, PA, USA, 2008; pp. 215–216.
8. Leyens, C.; Peters, M. *Titanium and Titanium Alloys*; Wiley-VCH: Weinheim, Germany, 2003.
9. Wu, X. Review of alloy and process development of TiAl alloys. *Intermetallics* **2006**, *14*, 1114–1122. [[CrossRef](#)]

10. Appel, F.; Paul, J.D.H.; Oehring, M. *Gamma Titanium Aluminide Alloys—Science and Technology*; Wiley-VCH: Weinheim, Germany, 2011.
11. Clemens, H.; Mayer, S. Design, processing, microstructure, properties, and applications of advanced intermetallic TiAl alloys. *Adv. Eng. Mater.* **2013**, *15*, 191–215. [[CrossRef](#)]
12. Appel, F.; Oehring, M.; Wagner, R. Novel design concepts for gamma-base titanium aluminide alloys. *Intermetallics* **2000**, *8*, 1283–1312. [[CrossRef](#)]
13. Cui, W.F.; Liu, C.M.; Bauer, V.; Christ, H.-J. Thermomechanical fatigue behaviours of a third generation γ -TiAl based alloy. *Intermetallics* **2007**, *15*, 675–678. [[CrossRef](#)]
14. Baur, H.; Joos, R.; Smarsly, W.; Clemens, H. γ -TiAl for aeroengine and automotive applications. In *Intermetallics and Superalloys*; Wiley-VCH: Weinheim, Germany, 2000; pp. 384–390.
15. Tetsui, T. Effect of composition on endurance of TiAl in turbocharger applications. In *Gamma Titanium Aluminides 1999*; Kim, Y.-W., Dimiduk, D.M., Loretto, M.H., Eds.; The Minerals, Metals and Materials Society (TMS): Warrendale, PA, USA, 1999; pp. 15–23.
16. Sommer, A.; Keijzers, G. Gamma TiAl and the engine exhaust valve. In *Gamma Titanium Aluminides 2003*; The Minerals, Metals and Materials Society (TMS): Warrendale, PA, USA, 2003; pp. 3–8.
17. Lasalmonie, A. Intermetallics: Why is it so difficult to introduce them in gas turbine engines? *Intermetallics* **2006**, *14*, 1123–1129. [[CrossRef](#)]
18. Clemens, H.; Bartels, A.; Bystrzanowski, S.; Chladil, H.F.; Leitner, H.; Dehm, G.; Gerling, R.; Schimansky, F.P. Grain refinement in γ -TiAl-based alloys by solid state phase transformations. *Intermetallics* **2006**, *14*, 1380–1385. [[CrossRef](#)]
19. Clemens, H.; Smarsly, W. Light-weight intermetallic titanium aluminides—Status of research and development. *Adv. Mater. Res.* **2011**, *278*, 551–556. [[CrossRef](#)]
20. Clemens, H.; Wallgram, W.; Kremmer, S.; Güther, V.; Otto, A.; Bartels, A. Design of novel β -solidifying TiAl alloys with adjustable β/β_0 -phase fraction and excellent hot-workability. *Adv. Eng. Mater.* **2008**, *10*, 707–713. [[CrossRef](#)]
21. Imayev, R.M.; Imayev, V.M.; Khismatullin, T.G.; Oehring, M.; Appel, F. New approaches to designing of alloys based on γ -TiAl + α_2 -Ti₃Al. *Rev. Adv. Mater. Sci.* **2006**, *11*, 99–108. [[CrossRef](#)]
22. Naka, S. Advanced titanium-based alloys. *Curr. Opin. Solid State Mater. Sci.* **1996**, *1*, 333–339. [[CrossRef](#)]
23. Clemens, H.; Chladil, H.F.; Wallgram, W.; Zickler, G.A.; Gerling, R.; Liss, K.-D.; Kremmer, S.; Güther, V.; Smarsly, W. In and ex situ investigations of the β -phase in a Nb and Mo containing γ -TiAl based alloy. *Intermetallics* **2008**, *16*, 827–833. [[CrossRef](#)]
24. Kainuma, R.; Fujita, Y.; Mitsui, H.; Ohnuma, I.; Ishida, K. Phase equilibria among α (hcp), β (bcc) and γ (L1₀) phases in Ti-Al base ternary alloys. *Intermetallics* **2000**, *8*, 855–867. [[CrossRef](#)]
25. Tetsui, T.; Shindo, K.; Kobayashi, S.; Takeyama, M. A newly developed hot worked TiAl alloy for blades and structural components. *Scr. Mater.* **2002**, *47*, 399–403. [[CrossRef](#)]
26. Tetsui, T.; Shindo, K.; Kaji, S.; Kobayashi, S.; Takeyama, M. Fabrication of TiAl components by means of hot forging and machining. *Intermetallics* **2005**, *13*, 971–978. [[CrossRef](#)]
27. Kremmer, S.; Chladil, H.F.; Clemens, H.; Otto, A.; Güther, V. Near conventional forging of titanium aluminides. In Proceedings of the 11th World Conference on Titanium, Kyoto, Japan, 3–7 June 2008; pp. 989–992.
28. Wallgram, W.; Schmoelzer, T.; Cha, L.; Das, G.; Güther, V.; Clemens, H. Technology and mechanical properties of advanced γ -TiAl based alloys. *Int. J. Mater. Res.* **2009**, *100*, 1021–1030. [[CrossRef](#)]
29. Huber, D.; Clemens, H.; Stockinger, M. Near conventional forging of an advanced TiAl alloy. *MRS Proc.* **2012**, *1516*, 23–28. [[CrossRef](#)]
30. Kestler, H.; Clemens, H. Production, processing and application of γ (TiAl)-based alloys. In *Titanium and Titanium Alloys*; Leyens, C., Peters, M., Eds.; Wiley-VCH: Weinheim, Germany, 2003; pp. 356–360.
31. Crofts, P.; Bowen, P.; Jones, I. The effect of lamella thickness on the creep behaviour of Ti-48Al-2Nb-2Mn. *Scr. Mater.* **1996**, *35*, 1391–1396. [[CrossRef](#)]
32. Maruyama, K.; Yamamoto, R.; Nakakuki, H.; Fujitsuna, N. Effects of lamellar spacing, volume fraction and grain size on creep strength of fully lamellar TiAl alloys. *Mater. Sci. Eng. A* **1997**, *239–240*, 419–428. [[CrossRef](#)]

33. Voisin, T.; Monchoux, J.-P.; Hantcherli, M.; Mayer, S.; Clemens, H.; Couret, A. Microstructures and mechanical properties of a multi-phase β -solidifying TiAl alloy densified by spark plasma sintering. *Acta Mater.* **2014**, *73*, 107–115. [[CrossRef](#)]
34. Jin, Y.; Wang, J.N.; Yang, J.; Wang, Y. Microstructure refinement of cast TiAl alloys by β solidification. *Scr. Mater.* **2004**, *51*, 113–117. [[CrossRef](#)]
35. Imayev, V.M.; Imayev, R.M.; Khismatullin, T.G. Mechanical properties of the cast intermetallic alloy Ti–43Al–7(Nb,Mo)–0.2B (at. %) after heat treatment. *Phys. Met. Metallogr.* **2008**, *105*, 484–490. [[CrossRef](#)]
36. Yang, J.; Wang, J.N.; Wang, Y.; Xia, Q. Refining grain size of a TiAl alloy by cyclic heat treatment through discontinuous coarsening. *Intermetallics* **2003**, *11*, 971–974. [[CrossRef](#)]
37. Schwaighofer, E.; Clemens, H.; Mayer, S.; Lindemann, J.; Klose, J.; Smarsly, W.; Güther, V. Microstructural design and mechanical properties of a cast and heat-treated intermetallic multi-phase γ -TiAl based alloy. *Intermetallics* **2014**, *44*, 128–140. [[CrossRef](#)]
38. Schwaighofer, E.; Rashkova, B.; Clemens, H.; Stark, A.; Mayer, S. Effect of carbon addition on solidification behavior, phase evolution and creep properties of an intermetallic β -stabilized γ -TiAl based alloy. *Intermetallics* **2014**, *46*, 173–184. [[CrossRef](#)]
39. Kastenhuber, M.; Rashkova, B.; Clemens, H.; Mayer, S. Enhancement of creep properties and microstructural stability of intermetallic β -solidifying γ -TiAl based alloys. *Intermetallics* **2015**, *63*, 19–26. [[CrossRef](#)]
40. Appel, F.; Lorenz, U.; Oehring, M.; Sparka, U.; Wagner, R. Thermally activated deformation mechanisms in micro-alloyed two-phase titanium aluminide alloys. *Mater. Sci. Eng. A* **1997**, *233*, 1–14. [[CrossRef](#)]
41. Scheu, C.; Stergar, E.; Schober, M.; Cha, L.; Clemens, H.; Bartels, A.; Schimansky, F.-P.; Cerezo, A. High carbon solubility in a γ -TiAl-based Ti–45Al–5Nb–0.5C alloy and its effect on hardening. *Acta Mater.* **2009**, *57*, 1504–1511. [[CrossRef](#)]
42. Staron, P.; Christoph, U.; Appel, F.; Clemens, H. SANS investigation of precipitation hardening of two-phase γ -TiAl alloys. *Appl. Phys. A* **2002**, *75*, 1–3. [[CrossRef](#)]
43. Staron, P.; Schimansky, F.-P.; Scheu, C.; Clemens, H. SANS study of carbon addition in Ti–45Al–5Nb. *MRS Proc.* **2011**, *1295*, 195–200. [[CrossRef](#)]
44. Schwaighofer, E.; Staron, P.; Rashkova, B.; Stark, A.; Schell, N.; Clemens, H.; Mayer, S. *In situ* small-angle X-ray scattering study of the perovskite-type carbide precipitation behavior in a carbon-containing intermetallic TiAl alloy using synchrotron radiation. *Acta Mater.* **2014**, *77*, 360–369. [[CrossRef](#)]
45. Abe, E.; Kumagai, T.; Nakamura, M. New ordered structure of TiAl studied by high-resolution electron microscopy. *Intermetallics* **1996**, *4*, 327–333. [[CrossRef](#)]
46. Shull, R.D.; Cline, J.P. High temperature X-ray diffractometry of Ti–Al alloys. *High Temp. Sci.* **1988**, *26*, 95–117.
47. Schloffer, M.; Schmoelzer, T.; Mayer, S.; Schwaighofer, E.; Hawranek, G.; Schimansky, F.-P.; Pyczak, F.; Clemens, H. The characterisation of a powder metallurgically manufactured TNM titanium aluminide alloy using complementary quantitative methods. *Pract. Metallogr.* **2011**, *48*, 594–604. [[CrossRef](#)]
48. Novoselova, T.; Malinov, S.; Sha, W.; Zhecheva, A. High-temperature synchrotron X-ray diffraction study of phases in a gamma TiAl alloy. *Mater. Sci. Eng. A* **2004**, *371*, 103–112. [[CrossRef](#)]
49. Watson, I.J.; Liss, K.-D.; Clemens, H.; Wallgram, W.; Schmoelzer, T.; Hansen, T.C.; Reid, M. *In situ* characterization of a Nb and Mo containing γ -TiAl based alloy using neutron diffraction and high-temperature microscopy. *Adv. Eng. Mater.* **2009**, *11*, 932–937. [[CrossRef](#)]
50. Liss, K.-D.; Yan, K. Thermo-mechanical processing in a synchrotron beam. *Mater. Sci. Eng. A* **2010**, *528*, 11–27. [[CrossRef](#)]
51. Liss, K.-D.; Bartels, A.; Schreyer, A.; Clemens, H. High-energy X-rays: A tool for advanced bulk investigations in materials science and physics. *Textures Microstruct.* **2003**, *35*, 219–252. [[CrossRef](#)]
52. Schmoelzer, T.; Liss, K.-D.; Staron, P.; Mayer, S.; Clemens, H. The contribution of high-energy X-rays and neutrons to characterization and development of intermetallic titanium aluminides. *Adv. Eng. Mater.* **2011**, *13*, 685–699. [[CrossRef](#)]
53. Kim, Y.-W. Effects of microstructure on the deformation and fracture of γ -TiAl alloys. *Mater. Sci. Eng. A* **1995**, *192*, 519–533. [[CrossRef](#)]
54. Swaminathan, S. Debye-Waller factors in off-stoichiometric γ -TiAl: Effect of ordering of excess Al atoms on Ti sites. *Philos. Mag. Lett.* **1996**, *73*, 319–330. [[CrossRef](#)]
55. Kim, Y.-W. Microstructural evolution and mechanical properties of a forged gamma titanium aluminide alloy. *Acta Metall. Mater.* **1992**, *40*, 1121–1134. [[CrossRef](#)]

56. Grinfeld, M.A.; Hezzledine, P.M.; Shoykhet, B.; Dimiduk, D.M. Coherency stresses in lamellar Ti–Al. *Metall. Mater. Trans. A* **1998**, *29A*, 937–942.
57. Hashimoto, K.; Kimura, M.; Mizuhara, Y. Alloy design of gamma titanium aluminides based on phase diagrams. *Intermetallics* **1998**, *6*, 667–672. [[CrossRef](#)]
58. Kimura, M.; Hashimoto, K. High-temperature phase equilibria in Ti–Al–Mo system. *J. Phase Equilibria* **1999**, *20*, 224–230. [[CrossRef](#)]
59. Qin, G.W.; Oikawa, K.; Sun, Z.M.; Sumi, S.; Ikeshoji, T.; Wang, J.J.; Guo, S.W.; Hao, S.M. Discontinuous coarsening of the lamellar structure of γ -TiAl-based intermetallic alloys and its control. *Metall. Mater. Trans. A* **2001**, *32*, 1927–1938. [[CrossRef](#)]
60. Reimers, W.; Pyzalla, A.R.; Schreyer, A.; Clemens, H. *Neutrons and Synchrotron Radiation in Engineering Materials Science—From Fundamentals to Application*, 2nd ed.; Wiley-VCH: Weinheim, Germany, 2008.
61. Sears, V.F. Neutron scattering lengths and cross sections. *Neutron News* **1992**, *3*, 29–37. [[CrossRef](#)]
62. Schmoelzer, T. Investigation of γ -TiAl Alloys by Means of Diffraction Methods. Ph.D. Thesis, Montanuniversität Leoben, Leoben, Austria, April 2012.
63. Liss, K.-D.; Whitfield, R.E.; Xu, W.; Buslaps, T.; Yeoh, L.A.; Wu, X.; Zhang, D.; Xia, K. *In situ* synchrotron high-energy X-ray diffraction analysis on phase transformations in Ti–Al alloys processed by equal-channel angular pressing. *J. Synchrotron Radiat.* **2009**, *16*, 825–834. [[CrossRef](#)] [[PubMed](#)]
64. Staron, P.; Fischer, T.; Lippmann, T.; Stark, A.; Daneshpour, S.; Schnubel, D.; Uhlmann, E.; Gerstenberger, R.; Camin, B.; Reimers, W.; *et al.* *In situ* experiments with synchrotron high-energy X-rays and neutrons. *Adv. Eng. Mater.* **2011**, *13*, 658–663. [[CrossRef](#)]
65. Schmoelzer, T.; Mayer, S.; Sailer, C.; Haupt, F.; Güther, V.; Staron, P.; Liss, K.-D.; Clemens, H. *In situ* diffraction experiments for the investigation of phase fractions and ordering temperatures in Ti–44 at. % Al–(3–7) at. % Mo alloys. *Adv. Eng. Mater.* **2011**, *13*, 306–311. [[CrossRef](#)]
66. Erdely, P.; Stark, A.; Clemens, H.; Mayer, S. *In situ* high-energy X-ray diffraction on an intermetallic β -stabilised γ -TiAl based alloy. *BHM Berg-und Hüttenmännische Monatshefte* **2015**, *160*, 221–225. [[CrossRef](#)]
67. Treusch, R. Radiation sources: Production and properties of synchrotron radiation. In *Neutrons and Synchrotron Radiation in Engineering Materials Science*; Reimers, W., Pyzalla, A., Schreyer, A., Clemens, H., Eds.; Wiley-VCH: Weinheim, Germany, 2008; pp. 97–112.
68. Daniels, J.E. Determination of directionally dependent structural and microstructural information using high-energy X-ray diffraction. *J. Appl. Crystallogr.* **2008**, *41*, 1109–1114. [[CrossRef](#)]
69. McCusker, L.B. Product characterization by X-ray powder diffraction. *Microporous Mesoporous Mater.* **1998**, *22*, 527–529. [[CrossRef](#)]
70. McCusker, L.B.; von Dreele, R.B.; Cox, D.E.; Louër, D.; Scardi, P. Rietveld refinement guidelines. *J. Appl. Crystallogr.* **1999**, *32*, 36–50. [[CrossRef](#)]
71. Spieß, L.; Teichert, G.; Schwarzer, R.; Behnken, H.; Genzel, C. *Moderne Röntgenbeugung*, 2nd ed.; Vieweg + Teubner: Wiesbaden, Germany, 2009.
72. Clemens, H.; Boeck, B.; Wallgram, W.; Schmoelzer, T.; Droessler, L.M.; Zickler, G.A.; Leitner, H.; Otto, A. Experimental studies and thermodynamic simulations of phase transformations in Ti–(41–45)Al–4Nb–1Mo–0.1B alloys. In Proceedings of MRS Fall Meeting, Boston, MA, USA, 1–5 December 2008; pp. 115–120.
73. Boeck, B. Untersuchung und Verifizierung des Quasibinären Zustandsdiagramms für β -erstarrende TNM-Legierungen auf Basis von Ti–(41–45)Al–4Nb–1Mo–0.1B. Diploma Thesis, Montanuniversität Leoben, Leoben, Austria, August 2008.
74. Schmoelzer, T.; Liss, K.-D.; Zickler, G.A.; Watson, I.J.; Droessler, L.M.; Wallgram, W.; Buslaps, T.; Studer, A.; Clemens, H. Phase fractions, transition and ordering temperatures in TiAl–Nb–Mo alloys: An *in* and *ex situ* study. *Intermetallics* **2010**, *18*, 1544–1552. [[CrossRef](#)]
75. Schloffer, M.; Iqbal, F.; Gabrisch, H.; Schwaighofer, E.; Schimansky, F.-P.; Mayer, S.; Stark, A.; Lippmann, T.; Göken, M.; Pyczak, F.; *et al.* Microstructure development and hardness of a powder metallurgical multi phase γ -TiAl based alloy. *Intermetallics* **2012**, *22*, 231–240. [[CrossRef](#)]
76. Grujicic, M.; Zhang, Y. Crystal plasticity analysis of the effect of dispersed β -phase on deformation and fracture of lamellar $\gamma + \alpha_2$ titanium aluminide. *Mater. Sci. Eng. A* **1999**, *265*, 285–300. [[CrossRef](#)]
77. Liss, K.-D.; Schmoelzer, T.; Yan, K.; Reid, M.; Peel, M.; Dippenaar, R.; Clemens, H. *In situ* study of dynamic recrystallization and hot deformation behavior of a multi-phase titanium aluminide alloy. *J. Appl. Phys.* **2009**. [[CrossRef](#)]

78. Sun, F.-S.; Cao, C.-X.; Kim, S.-E.; Lee, Y.-T.; Yan, M.-G. Alloying mechanism of beta stabilizers in a TiAl alloy. *Metall. Mater. Trans. A* **2001**, *32*, 1573–1589. [[CrossRef](#)]
79. Kim, S.; Smith, G.D.W.; Roberts, S.G.; Cerezo, A. Alloying elements characterisation in γ -based titanium aluminides by APFIM. *Mater. Sci. Eng. A* **1998**, *250*, 77–82. [[CrossRef](#)]
80. Kim, S.; Smith, G.D.W. AP-FIM investigation on γ -based titanium aluminides. *Mater. Sci. Eng. A* **1997**, *239–240*, 229–234. [[CrossRef](#)]
81. Yeoh, L.A.; Liss, K.-D.; Bartels, A.; Chladil, H.F.; Avdeev, M.; Clemens, H.; Gerling, R.; Buslaps, T. *In situ* high-energy X-ray diffraction study and quantitative phase analysis in the $\alpha + \gamma$ phase field of titanium aluminides. *Scr. Mater.* **2007**, *57*, 1145–1148. [[CrossRef](#)]
82. Liss, K.-D.; Bartels, A.; Clemens, H.; Bystrzanowski, S.; Stark, A.; Buslaps, T.; Schimansky, F.-P.; Gerling, R.; Scheu, C.; Schreyer, A. Recrystallization and phase transitions in a γ -TiAl-based alloy as observed by *ex situ* and *in situ* high-energy X-ray diffraction. *Acta Mater.* **2006**, *54*, 3721–3735. [[CrossRef](#)]
83. Hoelzel, M.; Gilles, R.; Schlapp, M.; Boysen, H.; Fuess, H. Monte Carlo simulations of various instrument configurations of the new structure powder diffractometer (SPODI). *Phys. B Condens. Matter* **2004**, *350*, 671–673. [[CrossRef](#)]
84. Gilles, R.; Hoelzel, M.; Schlapp, M.; Elf, F.; Krimmer, B.; Boysen, H.; Fuess, H. First test measurements at the new structure powder diffractometer (SPODI) at the FRM-II. *Z. Krist.* **2006**, *1*, 183–188. [[CrossRef](#)]
85. Drössler, L.M. Characterization of β -Solidifying γ -TiAl Alloy Variants Using Advanced *in* and *ex situ* Investigation Methods. Diploma Thesis, Montanuniversität Leoben, Leoben, Austria, October 2008.
86. Studer, A.J.; Hagen, M.E.; Noakes, T.J. Wombat: The high-intensity powder diffractometer at the OPAL reactor. *Phys. B Condens. Matter* **2006**, *385–386*, 1013–1015. [[CrossRef](#)]
87. Erdely, P.; Werner, R.; Schwaighofer, E.; Clemens, H.; Mayer, S. *In situ* study of the time-temperature-transformation behaviour of a multi-phase intermetallic β -stabilised TiAl alloy. *Intermetallics* **2015**, *57*, 17–24. [[CrossRef](#)]
88. Park, H.S.; Nam, S.W.; Kim, N.J.; Hwang, S.K. Refinement of the lamellar structure in TiAl-based intermetallic compound by addition of carbon. *Scr. Mater.* **1999**, *41*, 1197–1203. [[CrossRef](#)]
89. Klein, T.; Schachermayer, M.; Mendez-Martin, F.; Schöberl, T.; Rashkova, B.; Clemens, H.; Mayer, S. Carbon distribution in multi-phase γ -TiAl based alloys and its influence on mechanical properties and phase formation. *Acta Mater.* **2015**, *94*, 205–213. [[CrossRef](#)]
90. Kawabata, T.; Tadanoi, M.; Izumi, O. Effect of carbon and nitrogen on mechanical properties of TiAl alloys. *ISIJ Int.* **1991**, *31*, 1161–1167. [[CrossRef](#)]
91. Tian, W.H.; Nemoto, M. Effect of carbon addition on the microstructures and mechanical properties of γ -TiAl alloys. *Intermetallics* **1997**, *5*, 237–244. [[CrossRef](#)]
92. Christoph, U.; Appel, F.; Wagner, R. Dislocation dynamics in carbon-doped titanium aluminide alloys. *Mater. Sci. Eng. A* **1997**, *239–240*, 39–45. [[CrossRef](#)]
93. Appel, F.; Paul, J.D.H.; Oehring, M.; Fröbel, U.; Lorenz, U. Creep behavior of TiAl alloys with enhanced high-temperature capability. *Metall. Mater. Trans. A* **2003**, *34*, 2149–2164. [[CrossRef](#)]
94. Appel, F.; Fischer, F.D.; Clemens, H. Precipitation twinning. *Acta Mater.* **2007**, *55*, 4915–4923. [[CrossRef](#)]
95. Gabrisch, H.; Stark, A.; Schimansky, F.-P.; Wang, L.; Schell, N.; Lorenz, U.; Pyczak, F. Investigation of carbides in Ti–45Al–5Nb– x C alloys ($0 \leq x \leq 1$) by transmission electron microscopy and high energy-XRD. *Intermetallics* **2013**, *33*, 44–53. [[CrossRef](#)]
96. Wang, L.; Gabrisch, H.; Lorenz, U.; Schimansky, F.-P.; Schreyer, A.; Stark, A.; Pyczak, F. Nucleation and thermal stability of carbide precipitates in high Nb containing TiAl alloys. *Intermetallics* **2015**, *66*, 111–119. [[CrossRef](#)]
97. Hammersley, A.P.; Svensson, S.O.; Hanfland, M.; Fitch, A.N.; Häusermann, D. Two-dimensional detector software: From real detector to idealised image or two-theta scan. *High Press. Res.* **1996**, *14*, 235–248. [[CrossRef](#)]
98. Blackburn, M.J. Some aspects of phase transformations in titanium alloys. In *The Science, Technology and Application of Titanium*; Jaffee, R.I., Promisel, N.E., Eds.; Plenum Press: New York, NY, USA, 1970; pp. 639–642.
99. Denquin, A.; Naka, S. Phase transformation mechanisms involved in two-phase TiAl-based alloys—II. Discontinuous coarsening and massive-type transformation. *Acta Mater.* **1996**, *44*, 353–365. [[CrossRef](#)]
100. Margulies, L.; Lorentzen, T.; Poulsen, H.F.; Leffers, T. Strain tensor development in a single grain in the bulk of a polycrystal under loading. *Acta Mater.* **2002**, *50*, 1771–1779. [[CrossRef](#)]

101. Poulsen, H.F. An introduction to three-dimensional X-ray diffraction microscopy. *J. Appl. Crystallogr.* **2012**, *45*, 1084–1097. [[CrossRef](#)]
102. Margulies, L.; Winther, G.; Poulsen, H.F. *In situ* measurement of grain rotation during deformation of polycrystals. *Science* **2001**, *291*, 2392–2394. [[CrossRef](#)] [[PubMed](#)]
103. Lauridsen, E.M.; Schmidt, S.; Suter, R.M.; Poulsen, H.F. Tracking: A method for structural characterization of grains in powders or polycrystals. *Appl. Crystallogr.* **2001**, *34*, 744–750. [[CrossRef](#)]
104. Inui, H.; Matsumuro, M.; Wu, D.-H.; Yamaguchi, M. Temperature dependence of yield stress, deformation mode and deformation structure in single crystals of TiAl (Ti–56 at. % Al). *Philos. Mag. A* **1997**, *75*, 395–423. [[CrossRef](#)]
105. Ihara, K.; Miura, Y. Dynamic recrystallization in Al-single crystals revealed by synchrotron radiation Laue technique. *Mater. Sci. Eng. A* **2004**, *387–389*, 651–654. [[CrossRef](#)]
106. Miura, Y.; Ihara, K.; Fukaura, K. Dynamic recrystallization in Al single crystals revealed by rapid X-ray Laue method. *Mater. Sci. Eng. A* **2000**, *280*, 134–138. [[CrossRef](#)]
107. Stark, A.; Rackel, M.; Tankoua, A.T.; Oehring, M.; Schell, N.; Lottermoser, L.; Schreyer, A.; Pyczak, F. *In situ* high-energy X-ray diffraction during hot-forming of a multiphase TiAl alloy. *Metals* **2015**, *5*, 2252–2265. [[CrossRef](#)]
108. Liss, K.-D.; Clemens, H.; Bartels, A.; Stark, A.; Buslaps, T. Phase transitions and recrystallization in a Ti-46 at. % Al-9 at. % Nb alloy as observed by *in situ* high-energy X-ray diffraction. *MRS Proc.* **2007**. [[CrossRef](#)]
109. Liss, K.-D.; Stark, A.; Bartels, A.; Clemens, H.; Buslaps, T.; Phelan, D.; Yeoh, L.A. Directional atomic rearrangements during transformations between the α - and γ -phases in titanium aluminides. *Adv. Eng. Mater.* **2008**, *10*, 389–392. [[CrossRef](#)]
110. Yan, K.; Liss, K.-D.; Garbe, U.; Daniels, J.; Kirstein, O.; Li, H.; Dippenaar, R. From single grains to texture. *Adv. Eng. Mater.* **2009**, *11*, 771–773. [[CrossRef](#)]
111. Liss, K.-D.; Garbe, U.; Li, H.; Schambron, T.; Almer, J.D.; Yan, K. *In situ* observation of dynamic recrystallization in the bulk of zirconium alloy. *Adv. Eng. Mater.* **2009**, *11*, 637–640. [[CrossRef](#)]
112. Schmoelzer, T.; Liss, K.-D.; Rester, M.; Yan, K.; Stark, A.; Reid, M.; Peel, M.; Clemens, H. Dynamic recovery and recrystallisation during hot-working in an advanced TiAl alloy. *Pract. Metallogr.* **2011**, *48*, 632–642. [[CrossRef](#)]
113. Sahu, P. Lattice imperfections in intermetallic Ti–Al alloys: An X-ray diffraction study of the microstructure by the Rietveld method. *Intermetallics* **2006**, *14*, 180–188. [[CrossRef](#)]
114. Schwaighofer, E.; Clemens, H.; Lindemann, J.; Stark, A.; Mayer, S. Hot-working behavior of an advanced intermetallic multi-phase γ -TiAl based alloy. *Mater. Sci. Eng. A* **2014**, *614*, 297–310. [[CrossRef](#)]
115. Cha, L.; Clemens, H.; Dehm, G. Microstructure evolution and mechanical properties of an intermetallic Ti-43.5Al-4Nb-1Mo-0.1B alloy after ageing below the eutectoid temperature. *Int. J. Mater. Res.* **2011**, *102*, 1–6. [[CrossRef](#)]
116. Cha, L.; Scheu, C.; Clemens, H.; Chladil, H.F.; Dehm, G.; Gerling, R.; Bartels, A. Nanometer-scaled lamellar microstructures in Ti-45Al-7.5Nb-(0; 0.5)C alloys and their influence on hardness. *Intermetallics* **2008**, *16*, 868–875. [[CrossRef](#)]
117. Veeraraghavan, D.; Pilchowski, U.; Natarajan, B.; Vasudevan, V.K. Phase equilibria and transformations in Ti-(25–52) at. % Al alloys studied by electrical resistivity measurements. *Acta Mater.* **1998**, *46*, 405–421. [[CrossRef](#)]
118. Beschliesser, M.; Chatterjee, A.; Lorich, A.; Knabl, W.; Kestler, H.; Dehm, G.; Clemens, H. Designed fully lamellar microstructures in a γ -TiAl based alloy: Adjustment and microstructural changes upon long-term isothermal exposure at 700 and 800 °C. *Mater. Sci. Eng. A* **2002**, *329–331*, 124–129. [[CrossRef](#)]
119. Takeyama, M.; Kumagai, T.; Nakamura, M.; Kikuchi, M. Cooling rate dependence of the α_2/γ phase transformation in titanium aluminides and its application to alloy development. In *Structural Intermetallics 1993*; Darolia, R., Lewandowski, J.J., Liu, C.T., Martin, P.L., Miracle, D.B., Nathal, M.V., Eds.; The Minerals, Metals and Materials Society (TMS): Warrendale, PA, USA, 1993; pp. 167–176.
120. Zhu, H.; Seo, D.Y.; Maruyama, K.; Au, P. Effect of microstructural stability on creep behavior of 47XD TiAl alloys with fine-grained fully lamellar structure. *Scr. Mater.* **2005**, *52*, 45–50. [[CrossRef](#)]
121. Tang, J.; Huang, B.; Zhou, K.; Liu, W.; He, Y.; Liu, Y. Factors affecting the lamellar spacing in two-phase TiAl alloys with fully lamellar microstructures. *Mater. Res. Bull.* **2001**, *36*, 1737–1742. [[CrossRef](#)]

122. Droessler, L.M.; Schmoelzer, T.; Wallgram, W.; Cha, L.; Das, G.; Clemens, H. Microstructure and tensile ductility of a Ti–43Al–4Nb–1Mo–0.1B alloy. *MRS Proc.* **2009**, *1128*, 121–126.
123. Guyon, J.; Hazotte, A.; Bouzy, E. Evolution of metastable α phase during heating of Ti48Al2Cr2Nb intermetallic alloy. *J. Alloy. Compd.* **2015**, *656*, 667–675. [[CrossRef](#)]
124. Zhu, H.; Matsuda, J.; Maruyama, K. Influence of heating rate in $\alpha + \gamma$ dual phase field on lamellar morphology and creep property of fully lamellar Ti–48Al alloy. *Mater. Sci. Eng. A* **2005**, *397*, 58–64. [[CrossRef](#)]
125. Dehm, G.; Motz, C.; Scheu, C.; Clemens, H.; Mayrhofer, P.H.; Mitterer, C. Mechanical size-effects in miniaturized and bulk materials. *Adv. Eng. Mater.* **2006**, *8*, 1033–1045. [[CrossRef](#)]
126. Cha, L.; Clemens, H.; Dehm, G.; Zhang, Z. *In situ* TEM heating study of the γ lamellae formation inside the α_2 matrix of a Ti–45Al–7.5Nb alloy. *Adv. Mater. Res.* **2011**, *146–147*, 1365–1368.
127. Clemens, H.; Mayer, S. Micro- and nanostructure evolution in intermetallic titanium aluminides. In Proceedings of the Ti-2011—12th World Conference on Titanium, Beijing, China, 19–24 June 2012; Zhou, L., Chang, H., Lu, Y., Xu, D., Eds.; Science Press: Beijing, China, 2012; pp. 395–403.
128. Schwaighofer, E.; Schloffer, M.; Schmoelzer, T.; Mayer, S.; Lindemann, J.; Güther, V.; Klose, J.; Clemens, H. Influence of heat treatments on the microstructure of a multi-phase titanium aluminide alloy. *Pract. Metallogr.* **2012**, *49*, 124–137. [[CrossRef](#)]
129. Clemens, H.; Wallgram, W.; Schloffer, M. Method for Producing a Component and Components of a Titanium-Aluminum Base Alloy. US Patent 2011,0277,891 A1, 17 November 2011.
130. Bolz, S.; Oehring, M.; Lindemann, J.; Pyczak, F.; Paul, J.; Stark, A.; Lippmann, T.; Schrüfer, S.; Roth-Fagaraseanu, D.; Schreyer, A.; *et al.* Microstructure and mechanical properties of a forged β -solidifying γ TiAl alloy in different heat treatment conditions. *Intermetallics* **2015**, *58*, 71–83. [[CrossRef](#)]
131. Huber, D.; Werner, R.; Clemens, H.; Stockinger, M. Influence of process parameter variation during thermo-mechanical processing of an intermetallic β -stabilized γ -TiAl based alloy. *Mater. Charact.* **2015**, *109*, 116–121. [[CrossRef](#)]
132. Kim, Y. Ordered intermetallic alloys, part III: Gamma titanium aluminides. *JOM* **1994**, *46*, 30–39. [[CrossRef](#)]
133. Perdrix, F.; Trichet, M.F.; Bonnentien, J.L.; Cornet, M.; Bigot, J. Influence of cooling rate on microstructure and mechanical properties of a Ti–48Al alloy. *Intermetallics* **1999**, *7*, 1323–1328. [[CrossRef](#)]
134. Cao, G.; Fu, L.; Lin, J.; Zhang, Y.; Chen, C. The relationships of microstructure and properties of a fully lamellar TiAl alloy. *Intermetallics* **2000**, *8*, 647–653. [[CrossRef](#)]
135. Djanarthany, S.; Servant, C.; Penelle, R. Phase transformations in Ti₃Al and Ti₃Al + Mo aluminides. *J. Mater. Res.* **1991**, *6*, 969–986. [[CrossRef](#)]
136. Djanarthany, S.; Servant, C.; Penelle, R. Influence of an increasing content of molybdenum on phase transformations of Ti–Al–Mo aluminides—Relation with mechanical properties. *Mater. Sci. Eng. A* **1992**, *152*, 48–53. [[CrossRef](#)]
137. Schnitzer, R.; Chladil, H.F.; Scheu, C.; Clemens, H.; Bystrzanowski, S.; Bartels, A.; Kremmer, S. The production of lamellar microstructures in intermetallic TiAl alloys and their characterisation. *Pract. Metallogr.* **2007**, *44*, 430–442. [[CrossRef](#)]
138. Novoselova, T.; Malinov, S.; Sha, W. Experimental study of the effects of heat treatment on microstructure and grain size of a gamma TiAl alloy. *Intermetallics* **2003**, *11*, 491–499. [[CrossRef](#)]
139. Kenel, C.; Leinenbach, C. Influence of Nb and Mo on microstructure formation of rapidly solidified ternary TiAl–(Nb,Mo) alloys. *Intermetallics* **2016**, *69*, 82–89. [[CrossRef](#)]

